DESIGN, SYNTHESIS AND APPLICATION OF ELECTROSPUN HETEROSTRUCTURED NANOFIBERS FOR ELECTROCATALYTIC HYDROGEN EVOLUTION REACTIONS FROM WATER SPLITTING

A THESIS SUBMITTED TO
THE GRADUATE SCHOOL OF ENGINEERING AND SCIENCE
OF BILKENT UNIVERSITY
IN PARTIAL FULFILLMENT OF THE REQUIREMENTS FOR
THE DEGREE OF
MASTER OF SCIENCE
IN
MATERIALS SCIENCE AND NANOTECHNOLOGY

By

Elif Begüm Yılmaz

November 2021

ABSTRACT

DESIGN, SYNTHESIS AND APPLICATION OF ELECTROSPUN HETEROSTRUCTURED NANOFIBERS FOR ELECTROCATALYTIC HYDROGEN EVOLUTION REACTIONS FROM WATER SPLITTING

Elif Begüm Yılmaz

M.S. in Materials science and nanotechnology

Advisor: Dönüş Tuncel

November 2021

Environmental problems and climate changes have increased the importance of studies on the development of sustainable and clean energy methods that can be an alternative to energy production technologies using fossil fuels in recent years. Green hydrogen is environmentally friendly and a high-capacity energy carrier, as it does not cause any toxic by-products during its production. For this reason, attempts are being made to increase the efficiency of green hydrogen produced from water splitting. Development of the catalytic activities and stability of electrocatalysts has gained great importance in order to increase the performance of the hydrogen evolution reaction (HER). This study examines the effect of Ni/NiO-reduced graphene oxide catalysts fabricated in the form of heterostructured fibers by electrospinning on their intrinsic and extrinsic activities and their performance for HER. In order to examine the stability, activity and kinetics of the synthesized electrocatalyst, studies such as linear sweep voltammetry (LSV), electrochemical impedance spectroscopy (EIS), chronoamperometry (CA), were carried out and Tafel curves were interpreted. It has been observed that the optimal electrocatalyst exhibits outstanding electrocatalytic performance with an over potential of -212 mV at 10 mA cm^{-2}, and a Tafel slope of 90.6 mV dec^{-1} in alkaline electrolyte. Morphological and structural characterizations of electrocatalysts were investigated using X-ray diffraction (XRD), fourier transform infrared spectroscopy (FT-IR),

scanning electron microscopy (SEM), X-ray photoelectron spectroscopy (XPS), Raman spectroscopy, and transmission electron microscopy (TEM) methods.
Key words: electrospinning, nanofibers, hydrogen evolution reaction, water splitting, heterostructure, reduced graphene oxide, nickel

ÖZET

SU AYRIŞMASINDAN KAYNAKLANAN ELEKTROKATALİTİK HİDROJEN EVRİMİ REAKSİYONLARI İÇİN ELEKTRO-EĞİRİLMİŞ HETEROYAPILI NANOLİFLERİN TASARIMI, SENTEZİ VE UYGULAMASI

Elif Begüm Yılmaz

Malzeme Bilimi ve Nanoteknoloji, Yüksek Lisans

Danışman: Dönüş Tuncel

Kasım 2021

Çevre sorunları ve iklim değişiklikleri, son yıllarda fosil yakıtların kullanıldığı enerji üretim teknolojilerine alternatif olabilecek sürdürülebilir ve temiz enerji yöntemlerinin geliştirilmesine yönelik çalışmaların önemini artırmıştır. Yeşil hidrojen, üretimi esnasında hiçbir toksik yan ürüne sebep olmadığı için çevre dostudur ve yüksek kapasiteli bir enerji taşıyıcıdır. Bu nedenle su ayrıştırma yönteminden elde edilen yeşil hidrojen üretiminin verimini artırmaya yönelik bir çok çalışma yürütülmektedir. Hidrojen evrim reaksiyonunu (HER) geliştirmek adına elektrokatalizörlerin katalitik aktivitelerini ve stabilitelerini iyileştirmek büyük önem kazanmıştır. Bu çalışma, Ni/NiO-indirgenmiş grafen oksit heteroyapısının elektrospinning yöntemiyle nanofiber formda fabrikasyonunun katalizörün intrinsik ve ekstrinsik aktivitelerine etkisini ve bunun sonucunda ortaya koydukları HER performanslarını incelemektedir. Sentezlenen elektrokatalizörün stabilitesini, aktivitesini ve kinetiğini incelemek adına lineer süpürme voltametrisi (LSV), elektrokimyasal empedans spektroskopisi (EIS), kronoamperometri (CA) gibi çalışmalar yürütülmüş ve Tafel eğimleri yorumlanmıştır. Optimal elektrokatalizörün 10 mA cm^{-2} 'de -212 mV aşırı potansiyel ve 90.6 mv dec^{-1}'lik Tafel eğim değeri ile mükemmel elektrokatalitik performans sergilediği gözlemlenmiştir. Katalizörlerin morfolojik ve yapısal karakterizasyonları için X-ray kırınımı (XRD), fourier dönüşümlü kızılötesi spektroskopisi (FT-IR), taramalı elektron mikroskobu

(SEM), X-ray fotoelektron spektroskopisi (XPS), Raman spektroskopisi, ve geçirimli elektron mikroskobu (TEM) yöntemleri kullanılarak incelenmiştir.

Anahtar kelimeler: elektroeğirme, nanofiberler, hidrojen evrim reaksiyonu, su ayrışması, heteroyapı, indirgenmiş grafen oksit, nikel

Acknowledgement

I would like to extent my sincere gratitude to my supervisor, Assoc. Prof. Dönüş Tuncel, for providing support and guidance during my research that has greatly helped me to complete my master studies. I would like to express my thanks to the committee members for providing precious advice.

I appreciate all the faculty members and staff of UNAM for their help. I also thank Bilkent University for providing financial support to carry out my studies. I would like to thank Aysan Khaligh, Yasaman Sheidaei, and all the people I had the opportunity to work with in Prof. Tuncel's research group. I would like to express my special gratitude to Yasaman Sheidaei for her understanding, friendship, patience and always supporting me.

I am grateful to my family for the opportunities they have provided me throughout my life. I would like to thank all my dear friends who gave me motivation while carrying out my work. It wouldn't have been possible for my life to be this much fun without you. I would like to express my gratitude to my biggest supporter, who has always stood by me under all circumstances and did his best to help me. Words are not enough to describe the value you add to my life and your support. We were two people on this road.

With endless respect, love and gratitude to my most important source of inspiration, who guides my ideas and whose I try to follow.

Contents

List of Tables

List of Figures

List of Abbreviations

α	Charge transfer coefficient
b	Tafel slope (mV dec^{-1})
CA	Chronoamperometry
ECSA	Electrochemically active surface area
EDX	Energy dispersive X-ray analysis
EIS	Electrochemical impedance spectroscopy
ERGO	Electrochemically reduced graphene oxide
F	Faraday's constant (96485 C mol^{-1})
FTO	Fluorine doped tin oxide
FT-IR	Fourier transform infrared spectroscopy
GO	Graphene oxide
HER	Hydrogen evolution reaction
j	Current density (mA cm^{-2})
j_0	Exchange current density
LSV	Linear sweep voltammetry
N	Amount of hydrogen produced in moles
n	Number of electrons transferred
NF	Nanofiber
Ni	Nickel
NiO	Nickel oxide
NHE	Normal hydrogen electrode
rGO	Reduced graphene oxide
R	Resistance

R_{ct}	Charge transfer resistance
RHE	Reversible hydrogen electrode
R_s	Solution resistance
SEM	Scanning electron microscopy
T	Temperature (K)
TEM	Transmission electron microscopy
TGA	Thermogravimetric analysis
TOF	Turnover frequency
XPS	X-ray photoelectron spectroscopy
XRD	X-ray diffraction
Z	Impedance
Z'	Real part of impedance
Z"	Imaginary part of impedance
η	Overpotential
η @ 10 mA cm^{-2}	Overpotential at 10 mA cm^{-2}

Chapter 1

Introduction

1.1 Hydrogen for clean energy

In recent years, humanity has faced an energy crisis due to reasons such as the depletion of energy resources and the increase in environmental problems [1]. Today's energy technology is based on fossil fuels, which cause by-products such as carbon dioxide and carbon monoxide, which cause global warming and climate changes as a result of their use. The decrease in resources and the instability in security in the regions where oil reserves are located, the need to control environmental pollution necessitate the search for alternative fuels [3]. There have been attempts to develop many alternative fuels such as bio-diesel, LPG, hydrogen, boron, solar fuels. Compared to the other fuels mentioned, hydrogen has great potential for use as an alternative fuel due to its advantages such as being the most abundant element in our universe and having a high specific energy. For these reasons, it is aimed to produce hydrogen in almost unlimited quantities by using green energy produced from renewable sources [3]. Hydrogen is believed to have a high potential to contribute to sustainable development. A number of methods can be used for hydrogen production, such as thermochemical [4,5], electrochemical [6], photochemical [7], photocatalytic [8] or photo-electrochemical [9] processes. At the present time, hydrogen is obtained almost entirely using fossil fuel sources. For example, steam reforming of methane is currently one of the most widely used methods to obtain hydrogen from natural gas, producing almost 48% of hydrogen in this way [10].

Hydrogen produced from coal, on the other hand, meets 18% of the production need. Hydrogen production from biomass via pyrolysis can also be achieved [11-13].

Hydrogen can be produced using a much simpler method: electrolysis of water. Electrolysis is divided into two as alkaline electrolyte and polymer electrolyte membrane (PEM) [14]. It is accepted that the efficiency of alkaline water electrolysis is about 70-80% higher hydrogen value [15]. The net reaction for the production of hydrogen and oxygen by the water splitting process is:

$H_2O \rightarrow H_2 + ½\ O_2$ (Equation 1-1)

The illustration of water electrolysis for production of green hydrogen by three electrode cell configuration is shown in Figure 1.1.

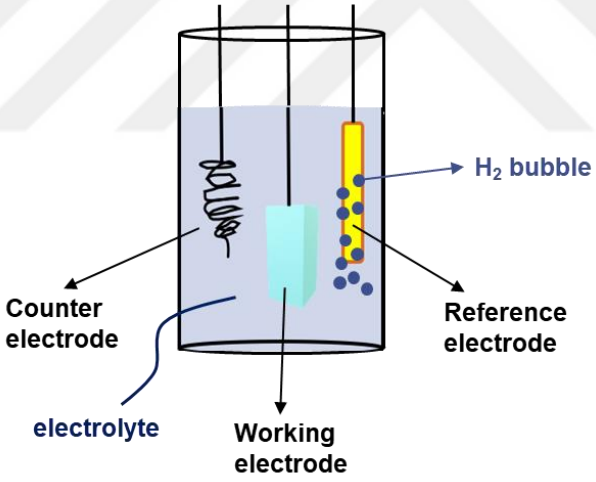

Figure 1.1 Illustration of hydrogen production by electrolysis.

1.2 Green hydrogen

Hydrogen can be obtained as a result of the use of various sources such as fossil fuels, nuclear energy, biomass and renewable energy sources and is categorized by labeling with different colors according to the production method (Figure 1.2).

Natural gas and methane are used as sources for gray hydrogen. This process produces only slightly fewer emissions than black and brown hydrogen, which uses bituminous or lignite coal in the hydrogen production process, meaning it is not environmentally friendly [16,17]. Black and brown are the ones that cause the most damage to the environment due to the CO_2 and CO produced in the production of hydrogen. When the carbon released during the process is captured or stored, it is called blue hydrogen and is also referred to as "low carbon" [18-20].

Green hydrogen is also called "clean hydrogen". It is produced by using clean energy obtained by utilizing renewable energy sources such as wind energy for splitting water through a process called electrolysis [21]. Green hydrogen refers to the production of hydrogen from the water electrolysis. Green hydrogen is obtained as a result of water splitting with the use of electricity produced from low-carbon sources.

Although it is environmentally friendly, the use of green hydrogen is very low at the present time due to its high production cost. However, the United States Department of Energy states that it expects the hydrogen market to grow as a result of the cost of hydrogen production falling from 6 $/kg in 2015 to 2 $/kg by 2025 [22,23].

Many industries now consider the use of green hydrogen as the most efficient way to ensure continuity, due to the intermittency of renewable energy sources [23]. This continuity can be achieved by storing energy when demand is low, and feeding excess energy back into the grid when demand for energy is increasing.

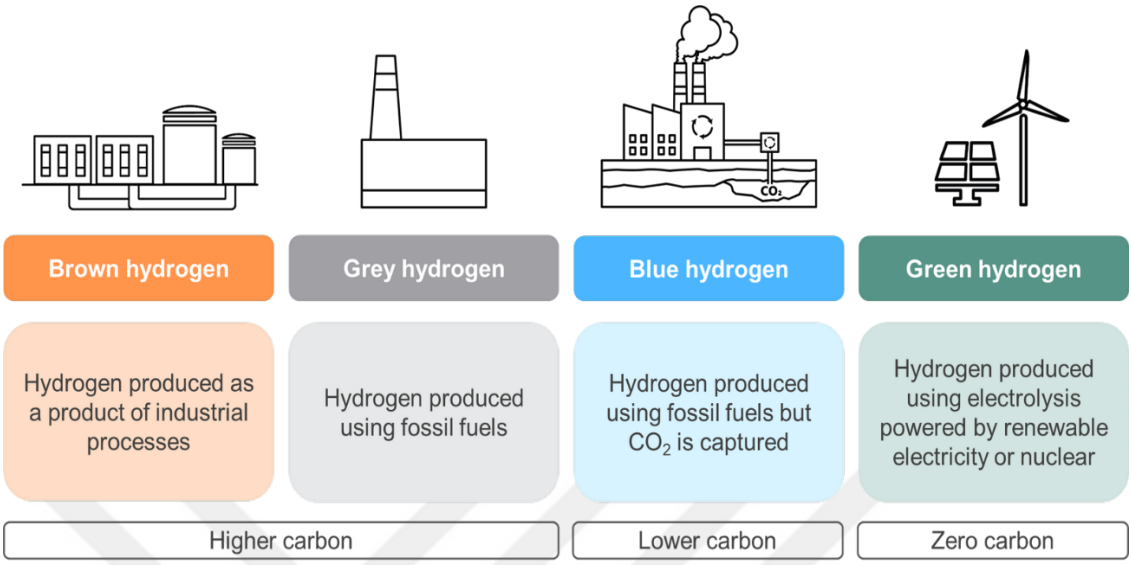

Figure 1.2 Visualization of brown, grey, blue and green hydrogen production methods and usage areas [18].

1.3 Water splitting

The water splitting is divided into two half-reactions called the hydrogen evolution reaction at the cathode (HER) and the oxygen evolution reaction at the anode (OER). A thermodynamic potential of 1.23 V and a Gibbs free energy (ΔG) of 273 kJ mol^{-1} are required for the dissociation of water with the reversible hydrogen electrode [24].
For basic medium:

Cathode (reduction): $2\ H_2O_{(l)} + 2e^- \rightarrow H_{2(g)} + 2\ OH^-_{(aq)}$ (Equation 1-2)
Anode (oxidation): $2\ OH^-_{(aq)} \rightarrow 1/2\ O_{2(g)} + H_2O_{(l)} + 2\ e^-$ (Equation 1-3)

For acidic medium:

Cathode (reduction): $2\ H^+_{(aq)} + 2e^- \rightarrow H_{2(g)}$ (Equation 1-4)
Anode (oxidation): $2\ H_2O_{(l)} \rightarrow O_{2(g)} + 4\ H^+_{(aq)} + 4e^-$ (Equation 1-5)

The Nernstian potential is calculated for each half-reaction at standard conditions of 25 °C and 1 atm, and even if it is found that a potential of 1.23 V is required to carry out the entire reaction, the actual value that must be applied to the electrolyzer is always higher. This value is called the overpotential (η) and is directly related to the cathode and anode materials and other resistors.

$$\eta = 1.23V + \eta_{anode} + \eta_{cathode} + \eta_{other} \quad \text{(Equation 1-6)}$$

In an electrochemical cell, the potential of the working electrode is measured relative to an electrode whose potential is known (reference electrode). The equilibrium potential of the reference electrode never changes (non-polarizable) throughout the experiment. Therefore, the changes in potential are considered to occur at the working electrode. It is very important to determine the potential scale when the thermodynamics of the reactions are pH dependent. Therefore, the measurements performed are written as a function of the Reversible Hydrogen Electrode (RHE), which also considers pH changes, instead of the Normal Hydrogen Electrode (NHE). The relationship between RHE and NHE is provided by the Nernst Equation:

$$E_{RHE} = E_{NHE} + 0.0059 \times pH \quad \text{(Equation 1-7)}$$

1.3.1 Hydrogen evolution reaction (HER) mechanism

HER is usually defined in two ways. These are hydronium ion reduction and water reduction as shown below:

$$2H_3O^+ + 2e^- \rightarrow H_2 + 2H_2O \quad \text{(Equation 1-8)}$$

$$2\ H_2O + 2e^- \rightarrow H_2 + 2\ OH^- \quad \text{(Equation 1-9)}$$

Hydronium ion reduction consists of three steps: Volmer (Equation 1-10), Heyrovsky (Equation 1-11) and Tafel steps (Equation 1-12). These are as follows:

$H_3O^+ + e^- + M \rightarrow M\text{-}H + H_2O$ Volmer step (Equation 1-10)

$M\text{-}H + H_3O^+ + e^- \rightarrow H_2 + H_2O + M$ Heyrovsky step (Equation 1-11)

$2M\text{-}H \rightarrow H_2 + M$ Tafel step (Equation 1-12)

The first step is known as Volmer and it can be simplified as:

$H^+ + e^- \rightarrow H_{ads}$ (Equation 1-13)

In the active site of the catalyst, the H^+ proton is bonded with an electron and is chemically absorbed onto the surface. There are two steps that are likely to occur after absorption: the Volmer-Tafel step and the Volmer-Heyrovsky step. The kinetics of these possible steps depend on the catalyst used and the applied potential. The Volmer-Tafel mechanism (or recombination mechanism) involves the production of hydrogen as a result of the combination of two H^+ protons adsorbed at two separate active sites on the surface.

$H_{ads} + H_{ads} \rightarrow H_2$ (Equation 1-14)

The Volmer-Heyrovsky mechanism, on the other hand, involves the formation of hydrogen as a result of the interaction of an H^+ adsorbed on the surface with an electron and a proton in the electrolyte.

$H_{ads} + H^+ + e^- \rightarrow H_2$ (Equation 1-15)

1.3.2 HER kinetics

HER kinetics are potential dependent and are described by the Butler-Volmer equation (Equation 1-16):

$j = j_0 [-e^{-\alpha nF\eta} + e^{(1-\alpha)nF\eta/R'T}]$ (Equation 1-16)

In this equation, j is the current density, j_0 is the exchange current density, n=1 is the number of transferred electrons, α is the charge transfer coefficient, F is Faraday's constant, η is the overpotential, R' is the ideal gas constant, and T is the temperature. j_0 defines the reaction rate at the equilibrium potential and can be used to evaluate electrocatalytic activity.

When the overpotential is small (η < 0.005 V), the Butler-Volmer equation can be rewritten as Equation 1-17.

$$\eta = RT/nFj0\ \varphi \qquad \text{(Equation 1-17)}$$

This equation shows that there is a linear relationship between the η and the logarithm of the current density (logj) in a narrow potential range close to equilibrium potential. At higher η (η>0.05 V), the Butler-Volmer equation is rewritten as the Tafel equation shown below:

$$\eta = a + b\log j = (-2.3RT)/nF\alpha\ \log j_0 + 2.3RT/nF\alpha\ \log j \qquad \text{(Equation 1-18)}$$

Equation 1-18 shows the linear relationship between the η and logj with a slope of $b = 2.3RT/nF\alpha$ called as Tafel slope.

1.3.2.1 Tafel slope

The Tafel value is used to determine the HER mechanisms and rate determining step. The Tafel slope shows the η increment required to increase the current density ten-fold. An ideal electrocatalyst is considered to have a small η and a low Tafel slope (b). Tafel analysis of linear sweep voltammetry curves can be done experimentally to obtain information about the kinetics. The Tafel slope and current density values are correlated, a good HER electrocatalyst is defined as one with a smaller overpotential at the intended current density. The value used to measure the electrocatalytic activities of HER

electrocatalysts is 10 mA cm^{-2}, that is equal to a solar to hydrogen efficiency of 12.3% [25].

Explaining the working mechanisms of different HER electrocatalysts is complicated. The Tafel slope can often be taken as an indication of which of the semi-reactions is the rate-determining step. Using Butler-Volmer kinetics, it can be deduced that the Tafel slopes are 120 mV/dec, 40 mV/dec, and 30 mV/dec, respectively, when the discharge reaction, electrochemical desorption reaction, or recombination reaction is the rate-determining step. If the Volmer reaction is RDS, then the α value is 0.5, which leads to a Tafel value of 120 mV/dec according to Equation 1-12. When RDS is Tafel half-reaction, the α value is 2 and the resulting Tafel value corresponds to 30 mV/dec. If the Heyrovsky half-reaction is RDS, the α value is 0.5, resulting in a Tafel slope of 40 mV/dec.

1.3.3 Turnover frequency

Turnover frequency (TOF) is a parameter used to understand how much reagent is transferred to the active sites in the catalyst per unit time. To calculate the TOF value, the total electrode activity is divided by the number of active sites on the surface. By using this value, the intrinsic activity of an active site can be interpreted [25]. The reason for obtaining this information is to compare the catalytic performances of catalysts. High TOF means the material has good catalytic activity. However, the calculation of the TOF value for heterogeneous catalysts is complicated because it is difficult to determine the number of active sites and their accessibility for these electrocatalysts. Cyclic voltammetry (CV) data recorded using certain scan rates over a certain potential window is used to calculate the number of active sites. The TOF value is calculated as:

$$TOF = I/(2Fn) \qquad \text{(Equation 1-19)}$$

In Equation 1-19, I respresents the current, n represents the number of active sites, and F is the Faraday's constant. n indicates that two electrons and two protons are required for a hydrogen molecule.

1.3.4 Transition metal (TM) / transition metal oxide (TMO) based heterostructured electrocatalysts

Platinum (Pt) is a state-of-the-art electrocatalyst for the hydrogen evolution reaction. However, due to its high cost and scarcity, it is not suitable for large scale production of hydrogen. Therefore, it is in great demand to find non-precious, earth-abundant and active catalysts that can replace Pt. Transition metal-based catalysts are an important alternative for HERs to replace noble metal-based catalysts due to their low cost and availability of active sites. However, metal oxide-based catalytic materials have a significant drawback; they have poor electronic conductivity, which hinders their use for HER. Most transition metal oxides are not preferred as catalysts for HER in acidic electrolytes (e.g. TiO_2, MoO_3, NiO) due to the lack of adsorption sites for H*. There are a number of transition metal oxide (TMO)-based heterostructures that can exhibit attractive HER activity in acidic solutions. The outstanding HER activities of transition metal hydroxide (TMH)-based heterostructures revealed its effective role in regulating water dissociation sites to produce alkaline HER catalysts. For example, CoO/Co_3O_4 heterostructured nanowires on titanium mesh were fabricated as an electrocatalyst and a low overpotential of ~108 mV @ 10 mA cm^{-2} were obtained at 1 M KOH for HER [26]. The amorphous Co_3O_4 structure may thought to facilitate the decomposition of water by promoting the activation of Lewis basic H_2O. In addition, oxygen vacancies also play an important role in increasing the adsorption of water, and the 3D structure facilitates bulk transport. Metallic Co, which has a very high conductivity, also allows fast electron transfer. With all this information, electrical conductivity correlates with size and morphology.

1.3.5 Nickel/nickel oxide-carbon (Ni/NiO-C) based electrocatalysts

Studies are being carried out to use Ni-based electrocatalysts as an alternative to Pt for HER, which is the half-reaction of the water splitting process required for clean energy

production, due to its chemical properties similar to Pt, having the same group number, and being cheap and abundant. Its good thermal and electrical conductivity, high corrosion resistance, and better ductility have made Ni-based materials widely used in electrochemical applications [27-28]. The good synergistic effect between Ni and neighboring heteroatoms provides improved surface adsorption properties, resulting in an increase in the catalytic properties of nanomaterials. The use of Ni and its derivatives can effectively increase the electrochemical active surface area for HER of nanomaterials in alkaline and acidic environments.

Nickel (Ni) is known as one of the best non-noble, cheap and earth-abundant catalysts for HER, although its stability has been criticized [29-34]. Nickel oxide (NiO), one of the transition metal oxides (TMOs) has been used as electrocatalysts in recent years due to their excellent activity and low production cost for OER in alkaline medium. Unfortunately, bulk NiO exhibits poor catalytic properties for HER due to its insufficient hydrogen adsorption energy. Many methods have been developed to overcome this situation. It has been stated that electrocatalytic Ni-based nanomaterials have high performance for HER and OER when synthesized on carbon nanostructures. Besides, it has been stated that electrocatalytic NiO-based nanomaterials have high performance for HER when synthesized on carbon nanostructures. For instance, Lu et al. investigated the electrocatalytic properties for HER by producing the NiO/C nanocomposite from the eggshell membrane and reported that the NiO/C nanocomposite outperformed pure NiO particles [35]. Subbaraman et al. reported that transition metal/metal oxide (M/MO) heterostructures played a reactive role for water splitting [36]. Considering the Ni/NiO heterostructure, Ni can convert hydrogen intermediates to H_2, while NiO can weaken the H-OH bond, thereby facilitating the dissociation of water. For example, Gong et al. synthesized the NiO/Ni-CNT heterostructure, and they reported greatly improved HER activity due to NiO species regulating the water dissociation step [37]. The NiO/Ni-CNT heterostructure demonstrated superior HER activity than NiO/CNT and Ni/CNT. The activity of Ni metal is low in basic medium, because OH^- ions can occupy sites required for H adsorption. Also, the NiO catalyst is not considered active for HER because there are no H_2 adsorption sites on the NiO electrode surface. Here, in the NiO/Ni-CNT, OH^- preferentially binds to the NiO region due to the strong electrostatic attraction of Ni^{2+} to

OH^-, while H^+ can be comfortably adsorbed on the Ni region on the catalyst surface. In addition, CNT plays a role in preventing agglomeration of Ni/NiO nanostructures while providing good electrical conductivity [38-40].

1.3.6 Reduced graphene oxide (rGO)

Graphene exhibits a densely packed monoatomic 2D sheet structure composed of sp^2-bonded carbon atoms [41-43]. Since its discovery in 2004, graphene has attracted attention for its use in various technological applications. Graphene oxide is electrically insulating because during the oxidation process of graphite, it acts as an electrical insulator due to the fact that a significant portion of the sp^2 carbon network is bonded with the oxygen-containing functional groups of graphite [44]. Electrical conductivity can be achieved by removing functional groups and restoring the original sp^2 electronic structure. For this purpose, graphene oxide needs to be reduced in order to regain the properties found in pristine graphene.

GO is usually made by oxidizing pure graphite and applying physical energy sequentially, such as sonication or mixing, thus allowing production with high efficiency and low costs [45,46] Due to this production method, the sp^2 bonding network of GO has a high defect density and disorder. Reduction of GO is required to provide the π network, which is the representative property of graphene [47,48] Reduction techniques can be categorized as chemical, thermal and electrochemical processes (Figure 1.3).

The reduced graphene oxide synthesis process by reduction of GO results in the formation of defective regions in rGO, and this defective structure provides larger surface area for rGO to be decorated with various functional groups. The inclusion of rGO, which has a conductive scaffold in the structure of electrocatalysts, provides various advantages such as improving catalyst performance. These properties of rGO allow the fabrication of composite materials because the dispersion of GO can be accomplished simply using certain solvents and facilitates hybridization with electroactive structures [49].

Liu et al. synthesized the Fe_2P@rGO nanowall arrays. The Fe_2P@rGO electrocatalyst demonstrated outstanding HER performance with an overpotential of 101 mV at 10 mA

cm^{-2} and a Tafel slope of 55.2 mV dec^{-1} [50]. This performance is due to the use of conductive rGO, which provides electron transfer with a large surface area. As another example, Ma et al. synthesized an N-doped carbon-coated CoP nanoparticles on N-doped graphene (CoP@NC-NG) using polyaniline (PANI) as a nitrogen source [51]. N-doped rGO used as support material prevented the aggregation of CoP NPs. CoP@NC-NG electrocatalysts showed superior HER activity, exhibiting an overpotential of 135 mV at 10 mA cm^{-2} and a Tafel slope of 59.3 mV dec^{-1} at 0.5 M H_2SO_4.

Figure 1.3 Structures of graphene oxide and reduced graphene oxide.

The chemical reduction method has a time-consuming procedure, the reducing agents used can contaminate the resulting product, but most importantly, it requires the use of chemicals that are harmful to the environment. Moreover, some of the oxygen functions in GO are selective and cannot be completely eliminated by a reductant treatment alone. On the other hand, the reduction of GO by thermal and electrochemical methods does not require the use of any harmful reducing agents, so they are relatively more environmentally friendly and faster [52,53]. For the electrochemical reduction of GO (ERGO), a standard electrochemical cell in an aqueous buffer solution is used. Oxygen functionalities in GO are eliminated by coating conductive solid films on the surface of a working electrode. The thermal reduction method involves the use of high temperatures to eliminate the oxygen functions. When heat treatment is applied (thermal reduction), carbonaceous groups in the form of carbon dioxide and carbon monoxide are removed

from GO. Moreover, a significant number of defects are induced in GO during thermal reduction as an output of the deoxygenation process [54-56].

1.3.7 Strategies to improve catalytic activity of an electrocatalyst

1.3.7.1 Intrinsic activity of a HER catalyst

Active site engineering of catalysts has made significant progress, but there are still limitations in electrode activities. The reason for this is that a small part of the active sites generally contributes to the reaction rate. Therefore, it is necessary to develop catalysts with higher intrinsic activity. The intrinsic activity is usually measured by the adsorption ability of the active sites of the catalysts. The adsorption energy can greatly reduce the overpotential required for HER. The tailored electron density at active sites provides enhanced chemical adsorption. For example, Chen et al. reported that the lattice mismatch between MoO_2-$MoSe_2$ in MoO_2@$MoSe_2$ nanolayers can produce rich structural defects in $MoSe_2$, which can provide many active sites for hydrogen evolution [57]. Thus, MoO_2 arrays exhibited a low onset potential at 63 mV, and a small Tafel slope value of 49 mV dec^{-1}.

The intrinsic catalytic activity of the active sites can be regulated by engineering the electronic structure of the electrocatalyst. It can be said that the intrinsic catalytic activity for HER is related to the electronic structure of metals [58]. Miles and Thomason observed that the intrinsic catalytic activity increases with the number of d-orbital electrons and decreases sharply with the filling of these d-orbitals [59]. According to their results, they stated that high catalytic activity was obtained for Ni, Pd and Pt, which have d^8s^2, $d^{10}s^0$ and d^9s^1 electronic configurations, respectively [59]. Many methods have been developed to increase the activity of electrocatalysts, such as increasing the number of active sites through structural engineering or providing more active sites. However, a small portion of the active sites contributes to the electrocatalytic reaction rate [60]. Also, limitations in mass/charge transport arise as a result of overloading catalysts on an electrode [61]. Therefore, additional methods have been developed that allow to increase

the intrinsic activity of the active sites by regulating their electronic structure (e.g. surface vacancy - defect, heterostructure engineering, strain regulation, heteroatom doping, phase transition).

The design of the heterostructure can create new catalytic domains by improving the charge transfer kinetics at the interfaces [10]. Thus, it is an important strategy for creating active interfaces for electrocatalysts. The heterostructure strategy optimizes the H* absorption behavior of the catalyst surface, thereby significantly improving the electrocatalytic activity [62,63]. As an example, Chen et al. synthesized a NiO/Ni heterostructure on carbon cloth (CC) by in situ surface reconstruction, which has a very high catalytic activity for HER [64].

1.3.7.2 Extrinsic activity of a HER catalyst

Studies have indicated that the catalytic activity of electrocatalysts is mainly dependent on the hydrogen atom adsorbed in the exposed edge sites [63]. Due to the limited number of active sites, catalytic activity is severely inhibited. Therefore, in order to improve their catalytic activity, it is desirable to design catalysts to have more active sites by optimizing their structures such as hollow structure, stepped surface structure, porous structure and nanostructuring. As an example, Faber et al. synthesized metallic pyrite phase CoS_2 with different film, microwire and nanowire morphologies on graphite disc/glass substrates by regulating the fabrication parameters of the catalyst for HER [65]. The group reported that catalyst morphology plays an important role in HER performance, and CoS_2 nanomaterials exhibit significantly enhanced HER catalytic activity due to the effect of the increased surface area of the electrode. In particular, it was stated that CoS_2 nanowire electrodes reached an overpotential of 145 mV @10 mA cm^{-2}.

Recently, rGO has been extensively investigated as a support for HER catalysts. Due to their high specific surface area (extrinsic effect), rGO layers increase the distribution of active sites, provide an efficient conductive network for electron transfer and improve catalyst stability. The greater the surface area of the catalyst, the more active site is available to participate in the reactions. In addition, electrospinning is a simple,

environmentally friendly and economical way of producing nanofibers with high specific surface area and porous structure. Since these combinations increase electron mobility and active sites, nanofibers have been used in HER as high efficiency electrocatalysts.

1.4 Electrospinning

Electrospinning is a technique that produces fibers ranging in diameter from nanometers to micrometers with an electric field applied to a polymer solution. Electrospinning is a very popular method for fiber production due to its cheapness, flexibility and ease of manufacture [66,67]. Multifunctional nanofibers can be produced because electrospun nanofibers are easily functionalized with nanoparticles, bioactive substances and additives [68].

A typical setup for the electrospinning process consists of three main components:

1. High voltage supplier: A direct current voltage of up to 30 kV is applied to produce electrospun fibers [69,70].
2. Nozzle capillary tube (small diameter needle): The nozzle is connected to a syringe containing the polymer solution. The syringe is connected to a pump so that the fluid flow rate can be controlled. The needle can also be connected vertically to the system, but it is usually used in a horizontal position to minimize the effect of gravity on drop formation. [70]
3. Metallic collector: Usually the collector is a conductive metal sheet. With this type of collecting sheet, nanofibers are usually deposited on the surface as a random mesh.

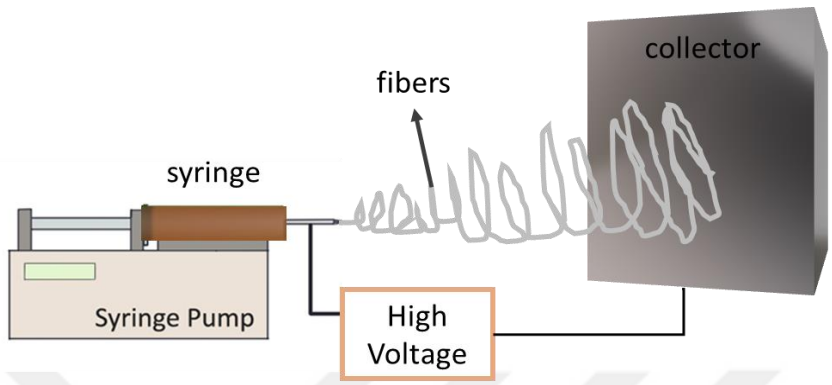

Figure 1.4 Scheme of the monoaxial electrospinning system

Monoaxial electrospinning is the simplest electrospinning experiment (Figure 1.4). The solution is dispensed through a single hole needle tip made of a conductive metal such as stainless steel, and this technique produces monolithic micro- or nano-sized fibers that are evenly and homogeneously blended. In compound jets (co-flowing jets), it is possible to use two, three or more liquids, and a more complex set of nozzles can be used to form complex structures of multiple polymers. The liquids used are loaded into different syringes and dispensed separately from each other using different syringe pumps.

In the coaxial electrospinning method, a coaxial needle is used, which consists of two concentrically arranged capillary channels. Each channel dispenses a polymer solution at separate flow rates. Since electrospinning is a fast-acting process, core/shell fibers with two separate divisions are obtained. Using three or more liquids also results in the production of three layers of more layered fibers [71].

1.4.1. Electrospinning parameters and defects

Many parameters can affect the conversion of polymer solutions into nanofibers by electrospinning. Apart from the molecular weight, viscosity, concentration and electrical conductivity of the precursor, the parameters in the system also affect the electrospinning. The solution feed rate, the voltage applied to the system, the distance

between the tip and the collector, the inner diameter of the needle, the type of collector, as well as environmental parameters such as temperature, relative humidity, pressure also affect the conversion properties of polymers to nanofibers [70]. Because of such variables involved in the electrospinning process, it is very difficult to predict the outcome of the experimental processes and some trial and error is required to obtain the desired nanofiber properties.

The most common defects that can be seen in electrospun nanofibers are electrospraying (Figure 1.5a) and pores (Figure 1.5b). These defects can be eliminated by changing the aforementioned parameters. In order to obtain as homogeneous nanofibers as possible, optimum parameters such as solution viscosity, solution feed rate, applied electric field, needle diameter should be determined.

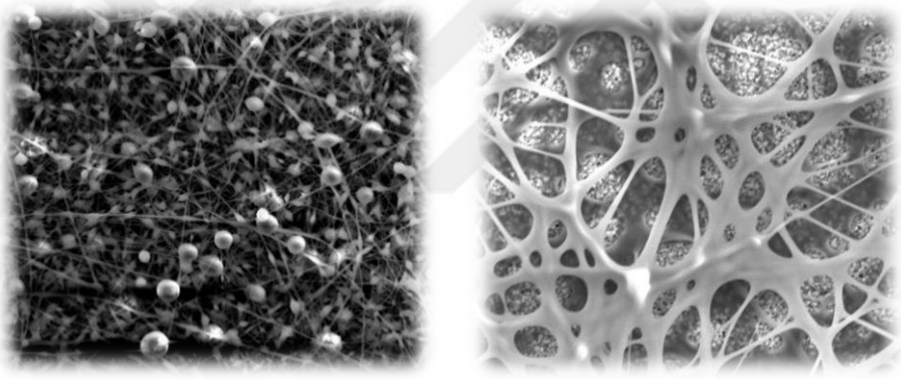

Figure 1.5 (a) beads-on string nanofibers as a result of electrospraying, (b) merged nanofibers

1.4.2 Applications of electrospun fibers

Electrospun fibers have significant potential for use in various applications due to their large surface-to-volume ratio and high porosity. Nano- and micro-sized fibers fabricated by electrospinning have been used in many applications (Table 1.1).

Table 1.1 Potential applications of electrospun nanofibers

Biomedical	**Filtration**	**Energy storage**
Drug delivery	Ion exchange membranes	Fuel cell
Wound dressing	Wastewater treatment	Solar cell
Antimicrobial membranes	Air filter porous membranes	Batteries
		Supercapacitors
		Anode material
Sensors	**Electrical**	**Textiles**
Chemical sensors	Actuators	Smart clothing
Fluorescence sensors	Nano interconnects	Protective clothing
Gas sensors		Fire retardant fabrics

The biomedical field is one of the most important application areas using the electrospinning technique. It is known that nanofibers are widely used for tissue engineering, drug release, wound dressing, enzyme immobilization. Nanofiber structures have been a superior performing material for membrane preparation in the fields of environmental engineering and bio-technology. These structures have been widely used for protein purification, wastewater treatment, enzymatic catalysis and synthesis etc. Polymer nanofibers are accepted as excellent membrane materials for defense and security purposes due to their light weight, breathable porous structure and high surface area [72]. Thus, various studies are being carried out to develop nanofiber surfaces in order to improve the decontamination and capture capabilities of warfare agents.

There is a need to develop clean energy sources which are environmentally friendly and can replace fossil sources. Fuel and photovoltaic cells, wind energy and geothermal energy generators are seen as possible alternative technologies. Likewise, due to their large surface area, polymer batteries, polymer electrolyte membrane fuel cells (PEMFCs) etc [73]. Studies are carried out for the use and development of electrospun

nanofiber membranes for It is desirable that polymer batteries be designed to replace the large-volume lithium batteries used in PC laptops and mobile phones. In addition, the large surface areas of nanofibers can increase ion conductivity. For this reason, polymer batteries produced from nanofiber membranes have a higher energy density/weight compared to conventional polymer batteries.

Fiber structures have potential for applications in lithium batteries, solar and fuel cells, supercapacitors, etc. For example, Kim et al. [74] fabricated a new polymer battery using porous PVDF nanofiber membranes. The porous structure promoted high lithium electrolyte intake to reduce electrolyte leakage, allowing for a larger amount of lithium electrolyte in thinner battery packs. Electrospinning is a very simple method to eliminate the limitations in electronic charge transfer and fabricate one-dimensional semiconductor nanowires and composite nanotubes used in nanophotonic/nanoelectronic device applications.

1.4.3 Electrospun fibers for water splitting

In electrolytic cells, electrical energy is used to decompose chemical compounds by electrolysis. Possible applications include electrochemical CO_2 reduction [75,76], water electrolysis [77-79], removal of heavy metals from wastewater by electrodeposition [80], nitrogen reduction [81] and nitrate removal [82]. Electrospun fibers can be used in many of these electrolytic cells due to their large surface-to-volume ratios. These fibers have improved electronic conductivity, specific surface area, and durability, thus making them a very promising candidate to be an electrocatalyst for HER. As an example, Chinnappan et al. produced C@NiO/Ni nanofibers by electrospinning in order to obtain an efficient electrocatalyst for HER in alkaline medium [83]. Mugheri et al. synthesized HER catalyst using NiO nanoparticles deposited on MoS nanofibers for water splitting [84]. For the precursor, they used NiO nanostructures together with ammonium phosphomolybdate hydrate and PVP solution. The fiber mat obtained by the electrospinning method was then subjected to calcination to eliminate the polymer. This electrocatalyst revealed good stability and high electrocatalytic activity in HER.

1.5. Aim of study

In this study, graphene oxide and nickel were designed as heterostructured nanofibers (NFs) for the first time using a monoaxial electrospinning system. Reduced graphene oxide/nickel/nickel oxide (rGO/Ni/NiO) catalyst was fabricated on the fluorine doped tin oxide (FTO) surface with a synthesis that took place in only two steps by thermal reduction of graphene oxide during calcination and removal of polyvinyl alcohol (PVA) from the fibers. Unlike studies in which transition metals or transition metal oxides and carbon support were combined, it was desired to increase the activity of our catalyst for HER by designing reduced graphene oxide/nickel/nickel oxide as heterostructure in nanofiber form. It is aimed to increase the catalyst performance by reducing the onset potential by using reduced graphene oxide instead of nanofibers in which carbon nanotubes are decorated with metals or carbon nanoparticles are in its structure. In addition, as a result of the synthesis of reduced graphene oxide at much lower temperatures compared to carbon nanotubes, it is aimed to save energy and to synthesize catalysts in a shorter time.

This study examines rGO/Ni/NiO heterostructured NFs as an efficient electrocatalyst for water splitting. The effects of strategies to increase the intrinsic activity and the number of electrochemical active sites on the catalyst activity were investigated by comparing the electrochemical behavior of rGO, Ni/NiO and rGO/Ni/NiO fibers for the hydrogen evolution reaction. Basically, electrocatalysts in nanofiber form were coated on the FTO surface by monoaxial electrospinning method and calcined and investigated in alkaline electrolyte. Parameters such as precursor concentration and components, electrode coating time, calcination temperature and time were optimized to increase the catalytic activity. During the calcination process, polyvinyl alcohol was eliminated and thermal reduction of graphene oxide was achieved. Subsequent studies focused on evaluating HER performances by comparing the catalytic activities and stability of our rGO, Ni/NiO NFs and rGO/Ni/NiO heterostructured catalyst with optimized percentages of its constituents. The synergistic effect between rGO and Ni/NiO and their effects on increasing the efficiency of the catalyst for HER were observed. All the above-mentioned steps were performed to determine the optimum sample for HER. This sample was then

characterized in detail using physical characterization methods such as X-ray diffraction (XRD), Fourier transform infrared spectroscopy (FT-IR), scanning electron microscopy (SEM) and energy dispersive X-ray analysis (EDX), X-ray photoelectron spectroscopy (XPS), Raman spectroscopy, and transmission electron microscopy (TEM) methods. The illustration of the simple and facile two step fabrication of rGO/Ni/NiO heterostructured nanofibers has shown in Figure 1.6. SEM images of nanofibers containing PVA/GO/Ni salt and rGO/Ni/NiO nanofibers obtained after thermal treatment are also included in this illustration.

To the best of our knowledge, this is the first report on the synthesis of rGO/Ni/NiO heterostructure by monoaxial electrospinning followed by calcination in only two steps and obtained in 1D nanofiber form. The presence of rGO will make electron transfer faster in the fiber and consequently improve the catalytic activity in HER. In addition, by means of its large active surface area, it prevents the agglomeration of Ni-based crystals, allow them to spread on the catalyst surface, thus improving the stability. The Ni/NiO heterostructure, on the other hand, will facilitate the splitting of water into hydrogen and hydronium ions, enabling the hydrogen ions to be adsorbed to the surface faster, thus improving the hydrogen formation kinetics. The use of graphene oxide and nickel salt, which is quite cheap, can increase the catalytic activity and reduce the cost.

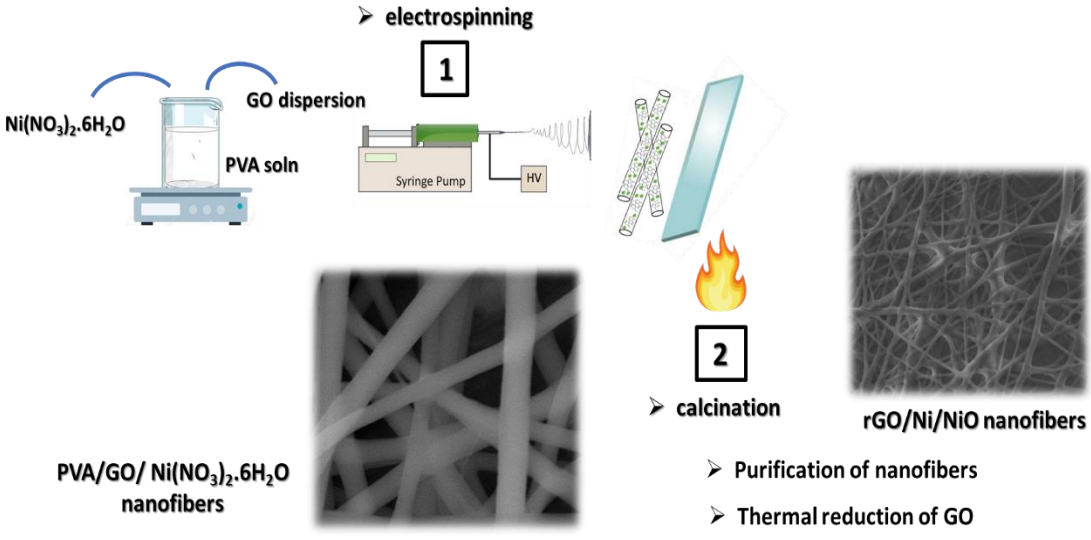

Figure 1.6 Illustration of fabrication steps of rGO/Ni/NiO electrocatalyst

Chapter 2

Experimental and instrumentation

2.1 Structural determination and characterization techniques

After the samples were synthesized, they were characterized using characterization methods such as thermogravimetric analysis (TGA), Fourier transform infrared spectroscopy (FT-IR), scanning electron microscopy (SEM), and X-ray diffraction (XRD) before electrochemical measurements. After choosing the optimum sample by making electrochemical measurements, the chemical structure and morphology of the sample has been characterized in detail using SEM, X-ray diffraction, transmission electron microscope (TEM), X-ray photoelectron spectroscopy (XPS), and Raman spectroscopy.

2.1.1 Raman spectroscopy

Raman spectroscopy is a method used to study changes in molecular state through radiation scattered from the sample. When monochromatic radiation probes a sample with an energy value that does not correspond to any electronic transition, this system switches from the ground state to an excited state. This transition introduces an unstable state that quickly returns with the emission of a photon of the same energy that probed the system. This interaction is called the Rayleigh component and corresponds to elastic scattering. A small part of the incident photons interacts inelastic. For this reason, they transfer or absorb some energy. The Stoke component of the spectrum results from situations where the emitted radiation has a lower energy than the first, while the Anti-

Stoke component results from situations where the emitted light has a higher energy than the first light.

The shift in frequency corresponds to the energy level of the vibrational and rotational mode of the molecule. Not all modes are Raman active, this is the case only for modes where lattice deformation means a change in polarizability.

Raman spectra were generated using the Horiba-Jobin-Yvon LabRam HR confocal microscope. Synapse CCD detector and 532 nm laser light are used in the device. Measurements were carried out in a range of 1000 - 2000 cm^{-1}.

2.1.2 Scanning electron microscopy (SEM) and energy-dispersive X-ray spectroscopy (EDX)

Scanning electron microscopy (SEM) is a method used to study the structure and composition of solid surfaces. In the SEM method, high-energy electrons are used to interact with the sample. This technique produces high-resolution images, giving information about the external morphology and chemical composition of the sample.

The electron beam is produced by heating a usually tungsten filament focused on a single beam, and the sample is probed inside the vacuum chamber. Since the image resolution increases with decreasing wavelength, the use of accelerated-therefore small wavelength electrons results in resolution in nm size. Accelerated electrons carry kinetic energy that is distributed in a variety of signals as a result of electron-sample interactions. As a result of the interaction of the primary electrodes with the atoms of the sample, the secondary (SE) and backscattered (BSE) electrons, and X-rays used for image generation are emitted. SE is caused by inelastic scattering as a result of the incident beam hitting the sample atoms. SE allows us to obtain information about the surface structure and morphology of the sample. BSE, on the other hand, results from the elastic interaction between the incident beam and the sample atoms. The resolution of the image of the sample obtained with BSE is weaker. The brightness of the image changes according to the atomic number. For example, heavy metals, i.e. elements with higher atomic number, appear brighter. That is, while SE provides detailed information about the image resolution, we obtain the morphological details in the image with BSE.

EDX measurements are made to analyze the chemical composition of the material. X-rays are formed by the outward movement of the inner cell electron as a result of excitation, and the resulting cavity being filled with an electron from the outer shell. With this transition, the energy difference created is emitted as an X-ray, and this energy difference is characteristic for atoms as it relates to the inner core electron energy levels. The morphology and composition of the samples were analyzed with the FEI Quanta 200 FEG ESEM instrument, which also provides Energy dispersive X-ray spectroscopy (EDX).

2.1.3 X-ray diffraction (XRD)

X-ray diffraction analysis (XRD) is a technique used to analyze the crystal structure of a material. XRD works on the principle of measuring the scattering angles and intensities of the X-rays leaving the material, following the incident X-rays sent to a material. XRD is a non-destructive technique used to examine the crystal phases and orientations and to determine structural properties.

Crystals are regular arrays of atoms. We can compare X-rays to waves of electromagnetic radiation. The atoms of the crystalline sample scatter the incoming X-rays through interaction as a result of the presence of electron clouds in their structure. This scattering is elastic. While these waves are divided into destructive interference and constructive interference, Bragg's law (Equation 2-1) benefits from constructive interference.

$$2d \sin\theta = n \lambda \qquad \text{(Equation 2-1)}$$

d is the spacing between the diffraction planes, θ is the incident angle, n is an integer, and λ is the wavelength of the beam. As a result, X-ray diffraction patterns are formed due to electromagnetic waves hitting a scattering array.

XPert Pro Multi-Purpose X-Ray Diffractometer was used to analyze the crystal structures of the samples. Cu Kα X-Ray Radiation (λ=1.542 Å) was used with a diffraction angle of 2θ = 4 - 80°, step size of 0.029, and time per step 500 s.

2.1.4 X-ray photoelectron spectroscopy (XPS)

X-ray photoelectron spectroscopy (XPS), (also known as electron spectroscopy for chemical analysis (ESCA)) is one of the methods used to analyze the sample surface. It is a frequently used to investigate the chemical composition, empirical formula, valence state of the elements of the sample surface. In XPS technique, low energy (~1.5 keV) X-rays used in the system to ionize molecules or atoms. If the hν value is larger, electrons can also be scattered from deeper levels. When the X-ray reaches the crystal surface, electrons are ejected from their valence shells. The XPS spectrum is obtained by measuring electrons e scaping from the surface. A high-resolution electron spectrometer is used to record the energy spectrum. Elements present in the sample can be identified from the kinetic energies of the photoelectrons. The relative concentrations of these elements can be found using their photoelectron densities.

Photon energies of X-rays are known. When these photons with known energies hit the surface, an electron is separated from the K_{shell} and the kinetic energy (KE) of this electron is examined in spectroscopy. The spectrum is basically plotted as a graph of the binding energy as a function of the electron counting rate. In other words, the XPS spectrum is a plot of the number of electrons detected relative to their kinetic energy. The binding energy is specific for each element. The kinetic energy of the ejected electrons can be formulated as:

$$KE = h\nu - BE \qquad \text{(Equation 2-2)}$$

hν is the energy of the photon, and BE is the binding energy of the atomic orbital from which the electron was launched. In the XPS spectrum, the inner orbital has a higher binding energy than the outer orbital. Thus, interactions occur between the incident photons and the atoms on the surface that cause photoelectric emission of electrons. Each element in the sample produces a unique set of XPS peaks in the characteristic binding energy values that directly describe it. These peaks correspond to the electronic configuration of electrons in different orbitals.

Thermo Scientific K-Alpha X-Ray Photoelectron Spectrometer was used for the analysis. The device is equipped with an Al Kα monochromator source operating at 400 mm spot size and hγ=14.866 eV.

2.1.5 Transmission electron microscopy (TEM)

Transmission electron microscope (TEM) device allows us to obtain comprehensive information about compounds and their structures by producing high quality images. The working principle of TEM is actually like a light microscope. However, there is a big difference between them, which is that light microscopes use beams of light to produce images, whereas TEM uses a beam of electrons to produce images.

Electrons have a shorter wavelength (about 0.005 nm) compared to light. Therefore, when the electron illuminates the sample, the wavelength of electron transmission increases, giving the TEM about 1000 times higher resolving power than that of a light microscope.

TEM can be used in a wide variety of fields such as nanotechnology, microbiology and forensic studies with the high-resolution power it produces. It has three working parts, including:

• electron gun
• image generating system
• image recording system

The electron beam sent from the electron gun is turned into a small and thin beam using the condenser lens. This electron beam hits the sample and its fragments are transmitted depending on parameters such as sample thickness. As electrons pass through the sample, they are scattered by the electrostatic potential from the elements in the sample. This transmitted portion is focused by the objective lens onto an image on the CCD camera. Darker areas of the image represent areas of the sample where less electrons are transmitted. Here, the Hitachi HT7700 TEM was used to further investigate the sample morphology and structure.

2.1.6 Fourier transform-infrared sectroscopy (FT-IR)

The fourier transform-infrared spectroscopy (FT-IR) analyzes the region with less frequency compared to the visible region. The theory is that bonds formed between different compounds are absorbed at different frequencies. The composition and structures of unknown samples can be identified by comparing spectrum with a reference spectrum database. Samples as small as 20 microns can be analyzed with FT-IR.

A device called an interferometer is used in the system to identify samples by generating an optical signal whose IR frequencies are encoded. The computer decodes the signal using a mathematical method called the Fourier transform, which then produces a mapping of the spectral information. This method offers a fast and cost-effective material analysis facility.

For the characterization of functional groups in the graphene oxide sample, Bruker Alpha Platimum ATR spectrometer was used to record Attenuated Total Reflection FT-IR Spectroscopy in the wavenumber range of 400 – 4000 cm^{-1}.

2.1.7 Thermogravimetric analysis (TGA)

Thermogravimetric analysis (TGA) records the change in weight of a material as a function of temperature (or time). It enables the analysis of the thermal stability of a material, the amount of solvent and moisture it contains, the filler content in polymers or the percent composition of components in compounds. Due to these properties, TGA is frequently used for analysis of decomposition temperature, performance of stabilizers, determination of low molecular weight monomers in polymers, moisture content of materials, residual solvent content, etc.

TGA is performed in an oven, usually in an Argon, Nitrogen or in dry air environment, by gradually increasing the temperature. A TGA graph is obtained by plotting the weight of our sample vs temperature (or time) to analyze thermal transitions in our sample, such as solvent loss in polymers, elimination of water from inorganic samples, or decomposition of materials. TGA is ideal for the determination of thermal properties of thermoplastics, thermosets, elastomers, mineral compounds, chemical and

pharmaceutical products. For analyzing the percent composition of components in samples, TGA was performed using TA Instruments Q500 thermogravimetric analyzer under dry air with a heating rate of 8 ^{o}C min^{-1}.

2.2 Experimental methods

2.2.1 Experimental setup

A three-electrode system is used to perform HER experiments. In order to accurately measure the potential of the working electrode, the reference electrode (non-polarizable) is used, which should have a well-defined potential. Commonly used reference electrodes are Ag/AgCl and Hg/HgO. The reference electrode is chosen according to the type of electrolyte used. Regardless of the reference electrode, all measured potentials must be converted to the RHE scale. The counter electrode (polarizable) should have no effect on the reaction taking place at the working electrode, should not affect the measurements, and must be calibrated with the working electrode. For these reasons, inert materials such as Pt or cheaper carbon cloth are used as counter electrodes [85].

Experiments in this study were performed with a three-electrode, single-cell setup as shown in Figure 2.1. Fluorine doped tin oxide (FTO) coated with electrospun nanofibers was used as the working electrode, Pt wire was used as the counter electrode, Ag/AgCl/KCl (sat.) solution was used as the reference electrode, and 1 M KOH solution was used as the electrolyte.

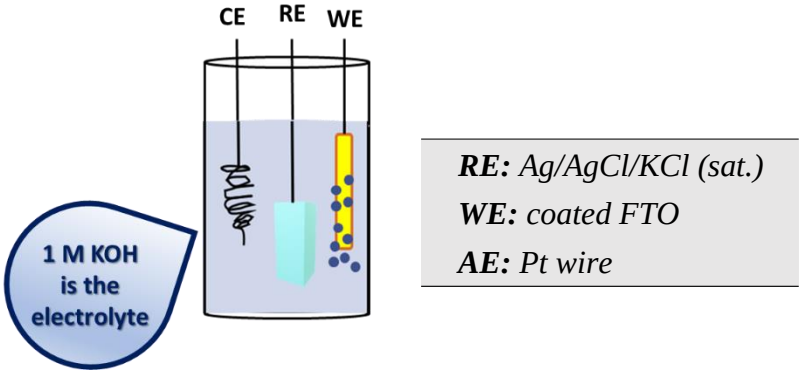

Figure 2.1 Three electrode cell configuration used for hydrogen production.

2.2.2 Linear sweep voltammetry (LSV)

The linear sweep voltammogram is the most common way to electrochemically test a system for reasons of speed and simplicity. If the initial potential is called E_1 during the measurement, it changes to its final value, which is E_2, as a function of time. The resulting current value in this process is summed up.

LSV (Figure 2.2) reveals the relationship of current recorded versus voltage applied during measurement, which can be better analyzed assuming that the kinetics of the oxidation reaction between A and B (reactant and product) is irreversible.

$$A_{(aq)} + e^- \rightleftharpoons B_{(aq)} \qquad \text{(Equation 2-3)}$$

At the beginning of the experiment, the potential value applied to the system is low. For this reason, the initial current is observed due to the migration of ions in the electrolyte. When the potential applied to the system reaches the reduction value, the type A on the surface begins to be reduced to B, thus more current begins to be recorded. As the potential continues to increase, the observed current increases exponentially with time.

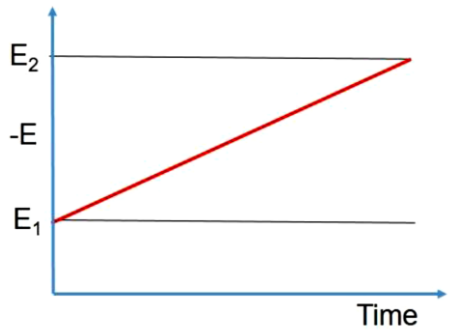

Figure 2.2 Potential sweep for an irreversible reaction.

2.2.3 Electrochemical impedance spectroscopy (EIS)

Electrochemical impedance spectroscopy (EIS) is performed to study electrode/electrolyte interface reactions. A current flowing in an electrical interface contains non-faradaic components due to electrochemical reactions.

$$O + ne^- \rightarrow R \qquad \text{(Equation 2-4)}$$

Here n is the number of transferred electrons, O is the oxidant and R is the reduced product. The electron is transferred across the electrical interface. Charge transfer results in both faradaic and non-faradaic components. The faradaic component results from the transfer of electrons through a reaction that takes place across the interface, crossing an appropriate activation barrier, i.e. polarization resistance, as well as uncompensated solution resistance. The non-faradaic current is the result of charging the double-layer capacitor (C_{dl}). The mass transfers of the reactant and product are involved in the consumption of oxidants and in determining the transfer rate of electrons [86].

The total impedance value is usually obtained by scanning the AC frequency in the range of 100 kHz ~ 10 mHz [87]. The frequency range of the EIS depends on the cell components and the typical response time. For this reason, the slow transport process, referred to as the Warburg impedance, is represented at a low frequency of 10 Hz to 10 mHz. Using typical time constants, faster transfer across the interface can be achieved in

the impedance associated with the charge transfer reaction, in the mid-frequency range from 10 kHz to 10 Hz, and the high frequency range from 100 kHz to 10 kHz. When V is applied with angular frequency ω, I and V have a phase difference of Ø. The values of V and I in the AC circuit can be expressed by the Equations 2-5 and 2-6. Here, V_m and I_m represent the maximum values of V and I, respectively.

$V = V_m\sin(\omega t)$ (Equation 2-5)

$I = I_m\sin(\omega t - Ø)$ (Equation 2-6)

If Equations 2-7 and 2-8 are modified using the complex function $j = \sqrt{-1} = \exp\frac{j\pi}{2}$;

$V = V_m\exp(j\omega t)$ (Equation 2-7)

$I = I_m\exp[j(\omega t - Ø)]$ (Equation 2-8)

V and I satisfy Ohm's law for the AC circuit model. Therefore, the impedance Z(ω) can be expressed as in Equation 2-9;

$$Z(\omega) = \frac{V(\omega)}{I(\omega)} = \frac{Vm\exp(j\omega t)}{Im\exp[j(\omega t - Ø)]} = \frac{Vm}{Im}\exp(jØ)$$ (Equation 2-9)

If Equation 2-9 is simplified using Euler's formula, $\exp(jØ) = \cos(Ø) + j\sin(Ø)$, it becomes:

$$Z(\omega) = \frac{Vm}{Im}\exp(jØ) = \frac{Vm}{Im}[\cos(Ø) + j\sin(Ø)] = Z_0[\cos(Ø) + j\sin(Ø)]$$ (Equation 2-10)

Equation 2-11 is obtained by dividing Equation 2-10 into real and imaginary parts:

$Z(\omega) = Z_0\cos(Ø) + Z_0\sin(Ø)j$ (Equation 2-11)

→$Z'_{real} = Z_0\cos(Ø)$: R(resistance)

→$Z''_{img} = Z_0\sin(Ø)$: C(capacitance) + L(inductance)

The EIS spectrum can be analyzed in two ways: 1) the Bode plot, which shows the magnitude changes or phase shift over a certain frequency range, and 2) the Nyquist plot, which shows the real and imaginary parts. Among these two graphs, the Nyquist graph is more often used to examine the properties of electrocatalysts because of the convenience it offers to analyze the active reaction mechanism.

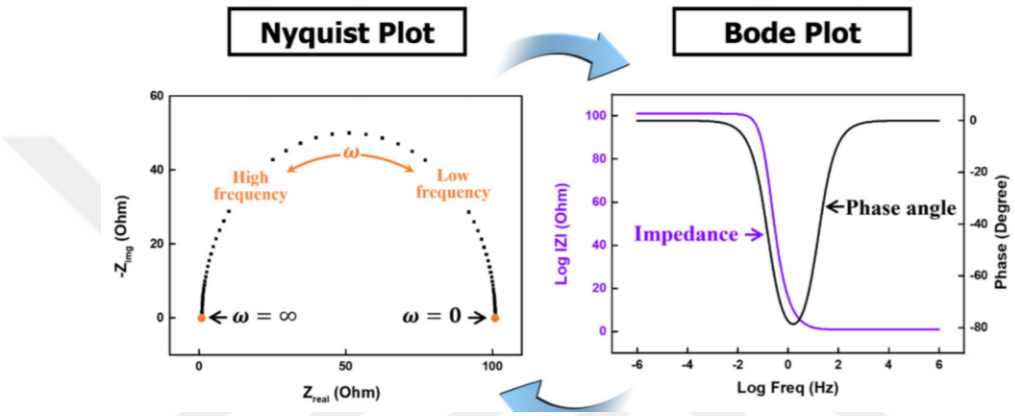

Figure 2.3 Impedance spectroscopy representation by Nyquist plot and Bode plot.

EIS circuit model consists of circuit elements such as resistors (R), capacitors (C), inductor (L). The capacitance value can be calculated using the peak point of the semicircle seen in the Nyquist plot. In the center of the semicircle, that is, at the point where Z_{img} is minimum, R_1 and ω values can be found from Equation 2-12 and the capacitance value can be easily calculated after this point.

$$\omega_{min} = 1/(R_1C_1) \qquad \text{(Equation 2-12)}$$

In the simplified Randles model, there is a double-layer capacitor with a bulk resistor (R_2) and a polarization resistor (R_1). The Nyquist plot of a simplified Randles model is shown in Figure 2.3. In this graph, the resistance of R_2 causes the starting point of the semicircle to shift towards higher Z_{real} values. The important point here is that the diameter of the semicircle corresponds to the load transfer resistance. Warburg impedance is used in equivalent circuit models where semi-infinite linear diffusion

affects a kinetic and diffusion-controlled system. The circuit model and Nyquist plot of this cell are shown in Figure 2.3. The Warburg impedance appears as a 45^{o} curved line under semi-infinite conditions [88].

2.2.4 Chronoamperometry (CA)

Chronoamperometry (CA) is a method in which a constant potential is applied over time to the working electrode (WE) and the current density obtained in response to this overpotential is plotted. The stability of electrocatalysts can be analyzed by applying a constant potential over a long period of time and observing the changes in current produced in response. The applied potential is chosen as a value at which the complete conversion of reactant (A) to product (B) is observed at the electrode. At the beginning of the measurement, a rapid decrease is observed in the graph due to rapid depletion of the A species near the electrode, after which the species to be reduced diffuses to the electrode. The lower the concentration gradient, the lower the current. Thus, the amount of fresh reagent approaching the surface is reduced.
The current response as a function of time is described using the Cottrell equation shown below.

$$|I| = \boldsymbol{nFAD^{1/2}[A_{bulk}]} / (\boldsymbol{\pi^{1/2}t^{1/2}}) \qquad \text{(Equation 2-13)}$$

n is the stoichiometric number of electrons involved in the reaction, I is the current, F is the Faraday constant, D is the diffusion constant for electroactive species, A is the electrode area and [A_{bulk}] is the initial concentration. The Cottrell equation is used to calculate the diffusion coefficient.

Chapter 3

Results and Discussion

3.1. Introduction

This chapter begins with a brief description of the synthesis and reduction methods of GO, the electrospinning of Ni/NiO, rGO and rGO/Ni/NiO heterostructured nanofibers, their physical and chemical characterizations. The electrochemical behavior of these nanofibers towards HER was investigated in alkaline electrolytes with different molarities, and a series of electrochemical measurements were performed after selecting the most suitable electrolyte by evaluating their electrocatalytic behaviors. Afterwards, the electrode was extensively characterized by methods such as X-ray diffraction, Raman spectroscopy, electron microscopy, and X-ray photoelectron spectroscopy. In the next step, the effect of adding GO to the precursor which contains Ni salt on HER activity was investigated. Then, the optimum composition was selected for HER by preparing solutions of various concentrations and using electrochemical measurements. In the light of electrochemical measurements, it was concluded that fabricating rGO/Ni/NiO heterostructured fibers enables better electrocatalytic activity and durability than Ni/NiO fibers. The structure and morphology of the electrode obtained from the spinning and calcination of this optimal composition were characterized. Comparing the activities of rGO nanofibers and rGO nanolayers, it was concluded that the rGO nanofibers showed better HER performance due to their larger active surface area. In addition, the electrocatalytic activities of the composite structure obtained by spinning rGO and Ni/NiO separately and the rGO/Ni/NiO heterostructure were compared and it was observed that the synergistic effect between rGO and Ni/NiO improved the HER activity.

3.2. Synthesis and characterization

3.2.1. Synthesis of graphene oxide

The first step of GO synthesis begins with the oxidation of graphite to obtain graphite oxide. Modified Hummer's method [89] is the most common method used for the oxidation of graphite. This method allows the oxidation of graphite in the presence of strong oxidants in a pH acidic environment.

All chemicals, graphite powder, $NaNO_3$, H_2SO_4, $KMnO_4$, H_2O_2, HCl were analytical reagent grade. The modified Hummers method was used for the preparation of graphene oxide. 2 g of graphite powder was oxidized together with 2 g of $NaNO_3$ in 92 mL of concentrated H_2SO_4. The mixture was then prepared in an ice bath and stirred on a magnetic stirrer for about 4 hours at a temperature not exceeding 5 °C. Approximately 12 g of $KMnO_4$ was slowly added to the mixture at intervals of 10 minutes and allowed to stir again for 1 hour. After heating the mixture to 35°C, it was cooled to room temperature. 180 mL of DDI water was added to the mixture at room temperature and stirred for 1 hour. After this time, the mixture was heated to 90°C with stirring for 2 hours, then 400 mL of DDI water was added. 48 mL of 30% H_2O_2 was added to the mixture to stop the reaction at some point. The illustration of synthesis procedure is shown in Figure 3.1.

The mixture was washed repeatedly with DDI water and 10% HCl and centrifuged at 5000 rpm for 12 minutes until the solution is reached to neutral pH, and allowed to settle for about 3 days. The centrifuge was stopped when the pH meter showed about 6-7. After centrifugation, the mixture was poured into glass beakers and dried at 50 °C, and the layers obtained in the beaker were powdered and prepared for use.

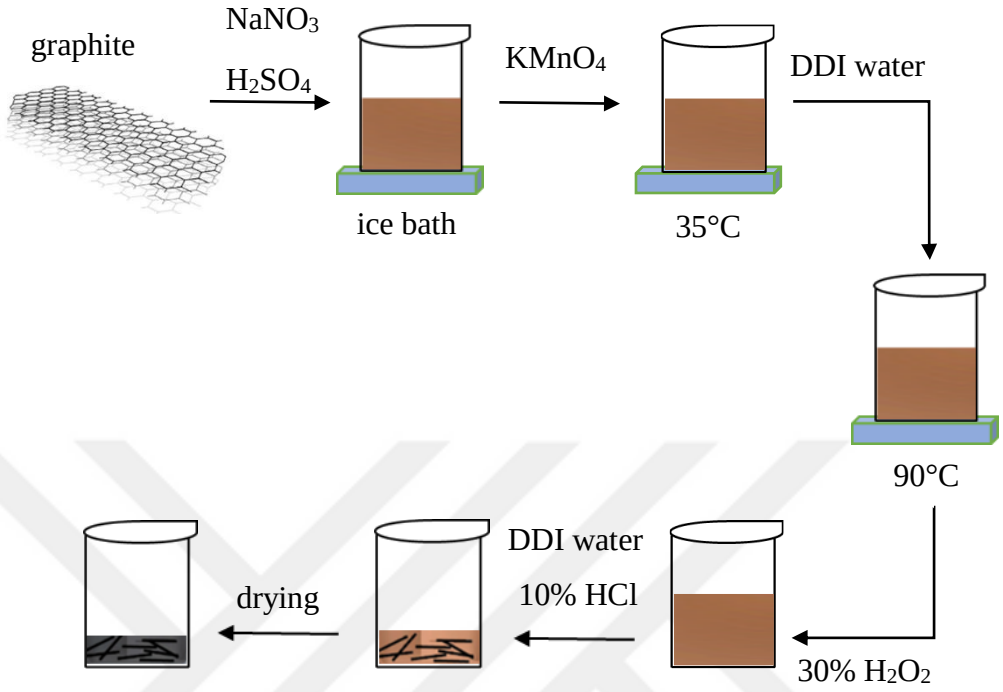

Figure 3.1 Synthesis of graphene oxide by modified Hummer's method

3.2.2. Characterization of graphene oxide

The FT-IR spectrum of GO powder confirmed an accomplished oxidation of graphite powder (Figure 3.2). The functional groups like C=O, C-OH, COOH and O-H were observed. In addition, a very broad peak between 3600 cm^{-1} and 2500 cm^{-1} was observed. It is due to the carboxyl O-H stretching mode [89-91]. The absorption peak corresponding to the O–H stretch (a peak of 3354 cm^{-1}) was observed as a result of the absorbed water and alcohol groups [90]. The peak corresponding to 2822 cm^{-1} is indicative of the CH_2 stretch of GO, while the peak around 1622 cm^{-1} corresponds to the C=C stretch in unoxidized graphite [91], the peak around 1730 cm^{-1} corresponds to the C=O stretch of the carboxyl group [89], 1225 cm^{-1} indicates the C-OH stretching of the alcohol group [92], and 1063 cm^{-1} to the C-O stretching vibrations [91].

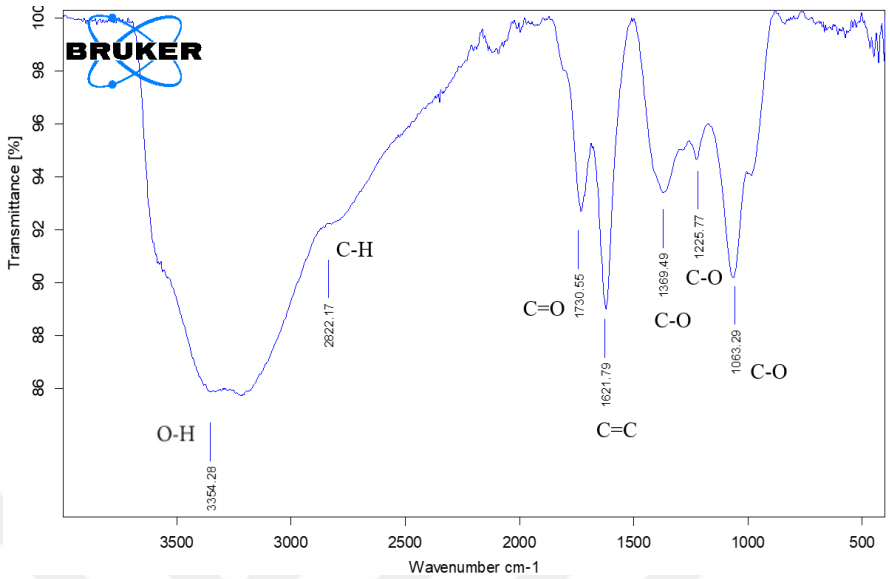

Figure 3.2. FT-IR spectra of graphene oxide powder

Figure 3.3 shows the X-ray diffraction pattern of GO powder. In the XRD model of GO synthesized by the modified Hummers method, it shows a peak at 2θ = 11° for the (001) crystal plane typical for GO, confirming successful GO synthesis [93]. The other peaks in this XRD pattern indicate the FTO crystal structure that has been used as a substrate.

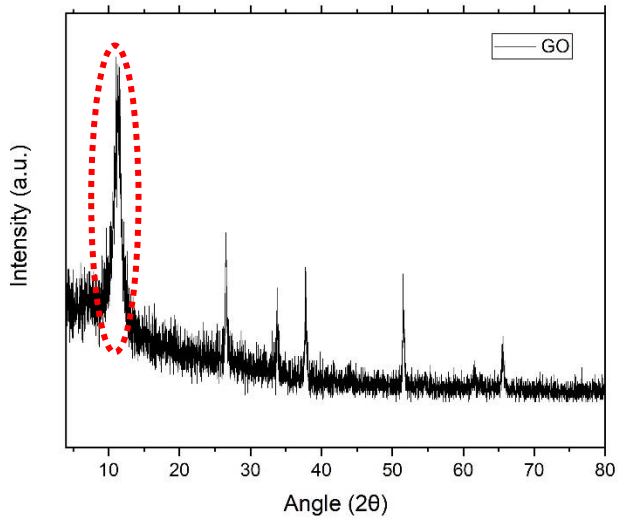

Figure 3.3. X-ray diffraction pattern of graphene oxide powder

3.2.3 Reduction methods of graphene oxide

3.2.3.1 Electrochemically reduced GO layers

For electrochemical reduction of GO (ERGO), FTO surface was coated with GO suspension (5 mg/mL) by drop casting method. GO suspension was sonicated for 30 min, then it was stirred in magnetic stirrer for 15 min to obtain a homogeneous solution. At first, 50 ml of GO dispersion was dropped onto the FTO surface. After the dispersion was dried at room temperature, 20 mL of Nafion was dropped on it to improve the stability of the surface. Cyclic voltammetry technique was used for ERGO. CV was performed at 0.5 M Na_2SO_4 with 20, 35 and 50 cycles between 0 V to -1.5 V (vs RHE) and at a scan rate of 50 mV/s to decide the optimum sweep segment for successful reduction of GO (Figure 3.4a-c).

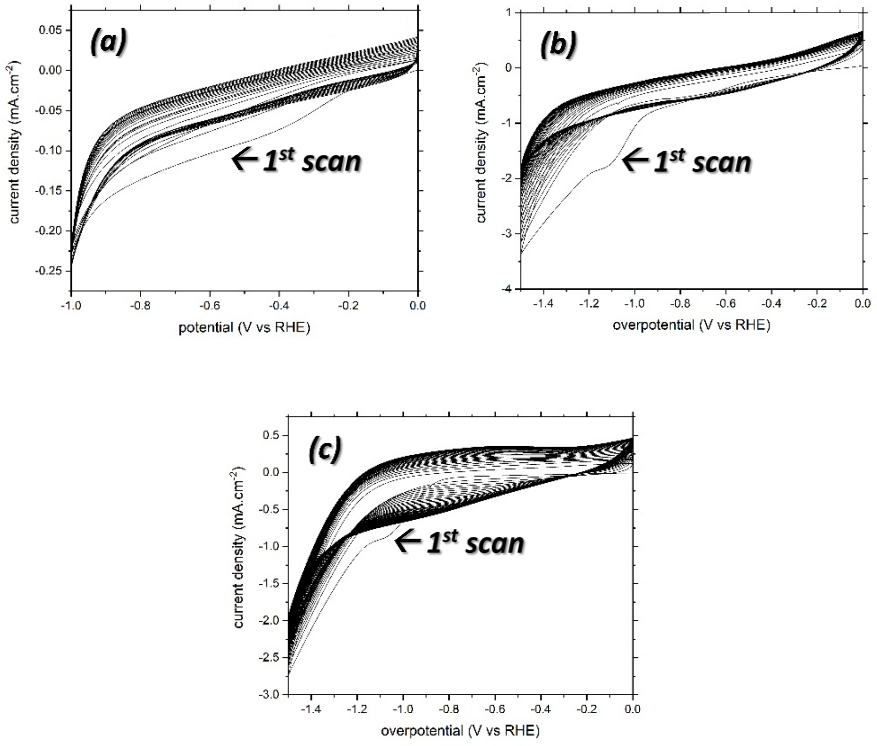

Figure 3.4. Cyclic voltammograms and number of cycles (a) 20 cycles, (b) 35 cycles, (c) 50 cycles for the reduction of GO layers onto FTO surface.

After lots of trials for the reduction of GO, it has been decided to perform the reduction process between 0 V to -1.5 V (vs RHE) and at a scan rate of 50 mV/s with 70 sweep segments. It can be seen from Figure 3.4a-c that there is a peak close to -1.0 V in the first cycle, but in the following cycles this situation has not been repeated. It means that there is no other reaction and the reduction process has finished successfully.

SEM characterization was performed for the morphological analysis of GO exposed to electrochemical reduction on the FTO surface. The SEM image of the electrochemically reduced graphene oxide nanolayers are shown in Figure 3.5.

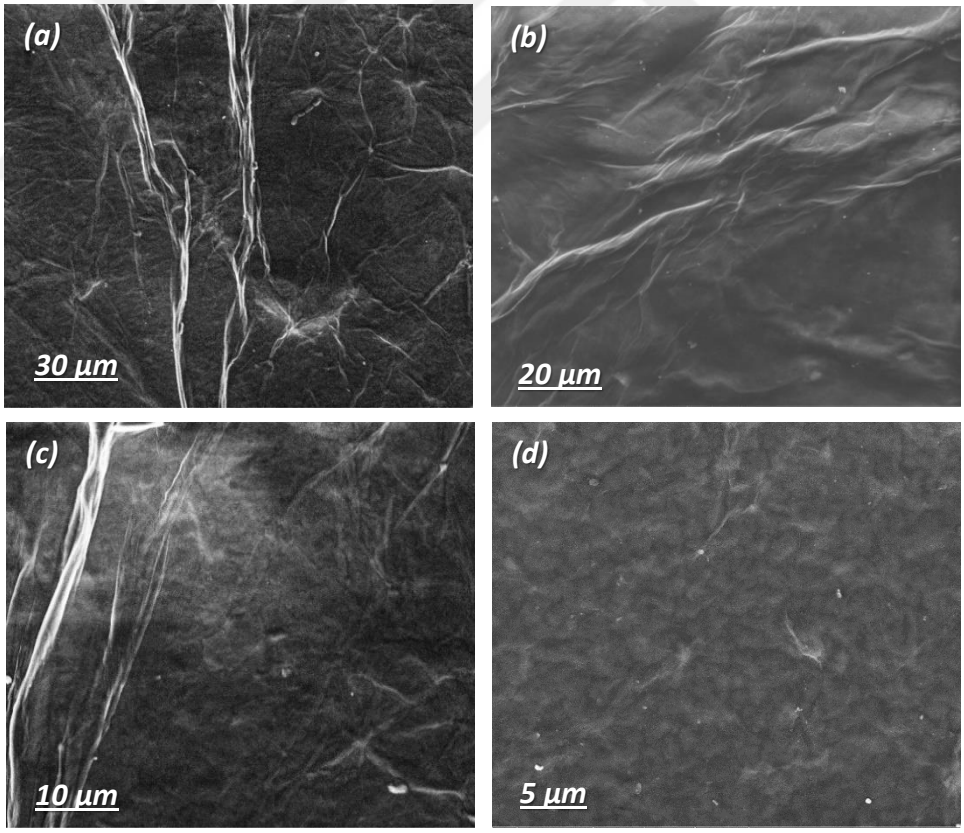

Figure 3.5. SEM images of electrochemically reduced GO layers onto FTO surface.

The layered structure of rGO is clearly visible in the SEM images (Figure 3.5a-c). A closer look at the rGO surface also reveals the roughness of the surface (Figure 3.5d). All these indicate that rGO promises a large surface area in electrochemical experiments. The electrochemical reduction method of the graphene oxide dispersion coated on the FTO surface by drop casting is illustrated in Figure 3.6.

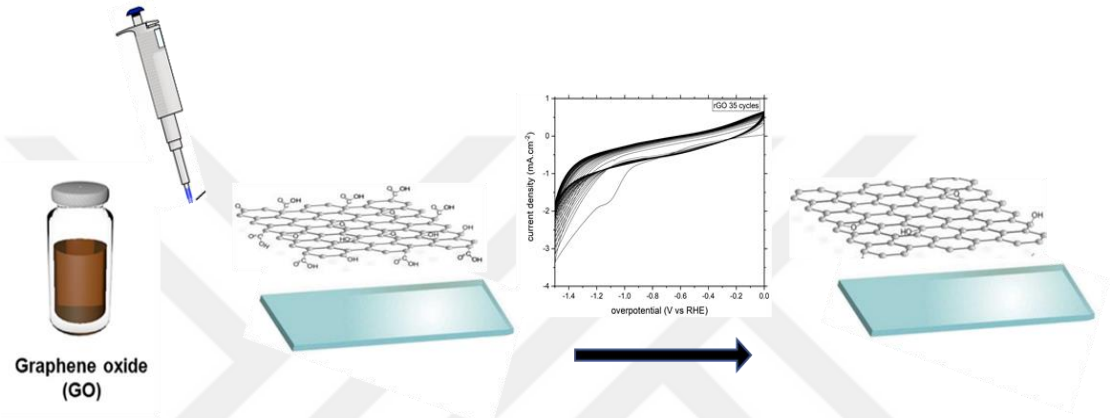

Figure 3.6. The diagram of the electrochemical reduction of graphene oxide.

As can be seen from the illustration, the GO structure before the CV experiment performed using the three-electrode cell configuration is visible on the FTO surface. After the CV technique in which 70 sweep segments were applied, it was seen that the functional groups were eliminated from the GO surface and rGO was synthesized.

The steps for ERGO synthesis can be summarized as follows:

- Preparation of GO suspension (5 mg/mL)
- Dropping the suspension onto the FTO surface and drying at room temperature
- Coating of Nafion on the GO surface
- Application of CV technique in 0.5 M Na_2SO_4 with 35 cycles
- Washing the electrode with ethanol and DDI water, respectively, and letting it dry at room temperature

3.2.3.2 Thermally reduced GO fibers

Thermal reduction method was applied on PVA/GO nanofibers obtained by electrospinning method. After coating FTO surface with PVA/GO fibers for 1 hour, these nanofibers were calcined at 340 ^{o}C for 1 hour. During calcination process, PVA polymer was eliminated from the electrode and GO was reduced applying high temperature. As a result, pure rGO nanofibers were obtained onto FTO surface.

Figure 3.7a shows the XRD spectra of PVA/GO and rGO nanofibers. A diffraction peak of around 12° appears at 2θ due to the penetration of oxygen-containing groups onto the graphite surface during GO synthesis [94]. As a result of thermal reduction, the diffraction peak at 12^{o} disappears and a new broad peak is observed around 2θ = 20°. This change in the shift peak indicates a decrease in GO. The shift towards a larger angle can be attributed to the reduced distance between the rGO interlayers [95]. Figure 3.7b shows the Raman spectra of PVA/GO and rGO nanofibers. It can be seen that the GO exhibits a prominent G-band (1580 cm^{-1}) and D-band (1350 cm^{-1}). The D-band is attributed to the respiration mode of the sp^2 carbon. In the rGO obtained after reduction, there are new sp^2 carbon atoms smaller in size than the sp carbon atoms found in GO. Therefore, the average crystallite size of sp^2 domains showed a reduction in rGO compared to GO and indicates the removal of oxygen groups.

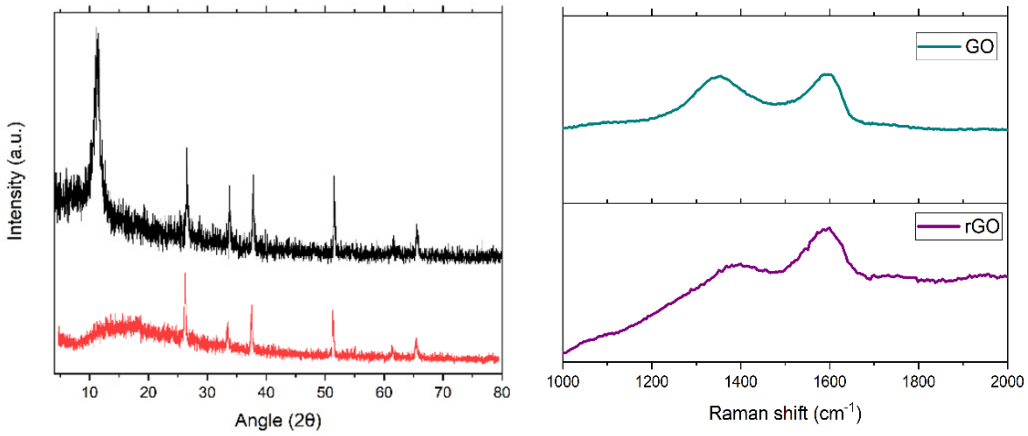

Figure 3.7. (a) XRD pattern and (b) Raman spectra of PVA/GO and rGO nanofibers.

As a result of thermal reduction of GO, rGO nanofibers were obtained from as-spun PVA/GO nanofibers. The fibers obtained as a result of purification of the fibers from PVA are shown in Figure 3.14. The fibers have a reticulated and interlocking structure.

3.2.4 The optimum synthesis method

The FTO substrate was first coated with GO dispersion by drop casting method. Then, rGO layers were obtained by electrochemical reduction using the cyclic voltammetry technique. On top of this layer, the solution containing PVA/Ni salt was coated on the rGO nanolayer in nanofiber form by applying high voltage. The fibers were then calcined at high temperature to remove PVA. The scheme of the synthesis procedure of rGO layer - Ni/NiO composite electrocatalyst is shown in Figure 3.8. The electrochemical reduction of the GO surfaces shown in Figure 3.8a is explained in detail in Section 3.2.3.1. The coating of the obtained rGO surface with Ni nanofibers is illustrated in Figure 3.8b.

(a)

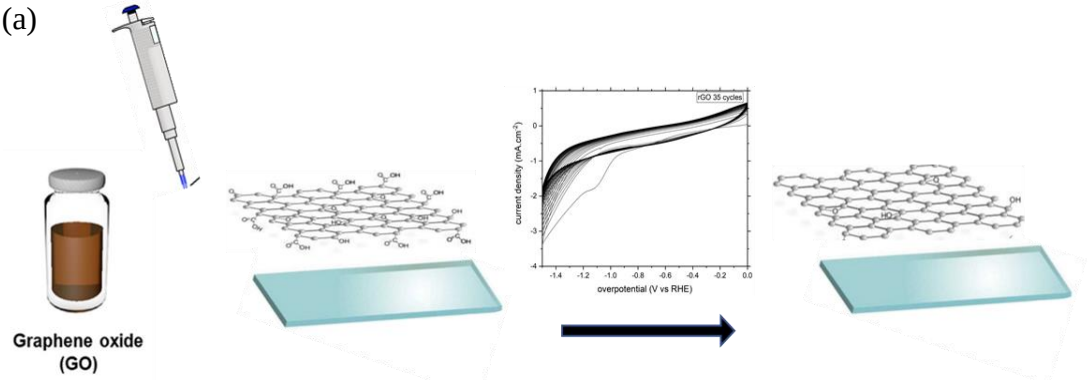

(b)

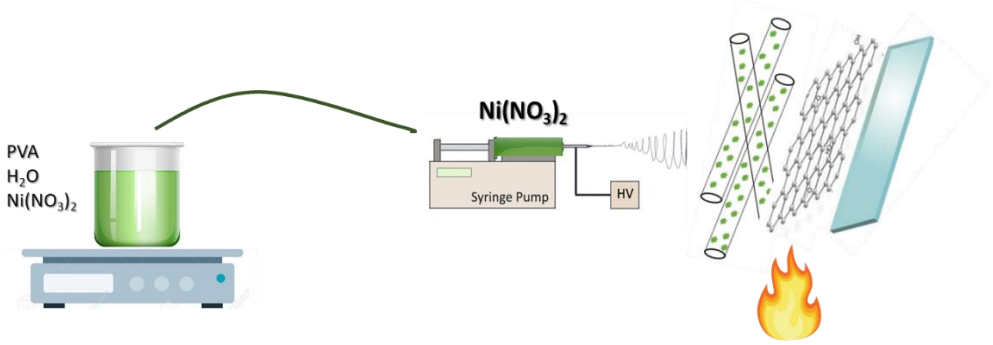

Figure 3.8 (a) electrochemical reduction of GO layers on FTO substrate, and (b) coating GO layer with PVA/$Ni(NO_3)_2.6H_2O$ fibers by electrospinning technique.

Figure 3.8b can be summarized as follows:

- Reduction of the GO surface as in Section 3.2.3.1
- Coating of PVA/Ni salt precursor on rGO layer using monoaxial electrospinning technique
- Fabrication of rGO layer- Ni/NiO nanofiber composite by eliminating PVA by calcination technique

However, this was a synthesis that took place in many steps and therefore was time consuming. In addition, when the rGO surface was exposed to high temperature, some parts of the rGO layers onto FTO surface were peeled off. In addition, Nafion, which was used to ensure the stability of rGO on the FTO surface, made it difficult to coat the nanofibers on the surface, as it slightly reduced the electrical conductivity of the rGO layer. Therefore, the idea of co-spinning GO and Ni salt was developed. Fabrication of the electrocatalyst consisted of only two steps, as rGO was obtained by thermal reduction of GO during the calcination process.

(i) ***electrospinning*** - synthesis of as-spun fibers (PVA/GO, PVA/ $Ni(NO_3)_2.6H_2O$, and PVA/GO/ $Ni(NO_3)_2.6H_2O$)

(ii) ***calcination*** - fabrication of rGO, Ni/NiO and rGO/Ni/NiO nanofibers

The illustration of synthesis procedure is shown in Figure 3.9.

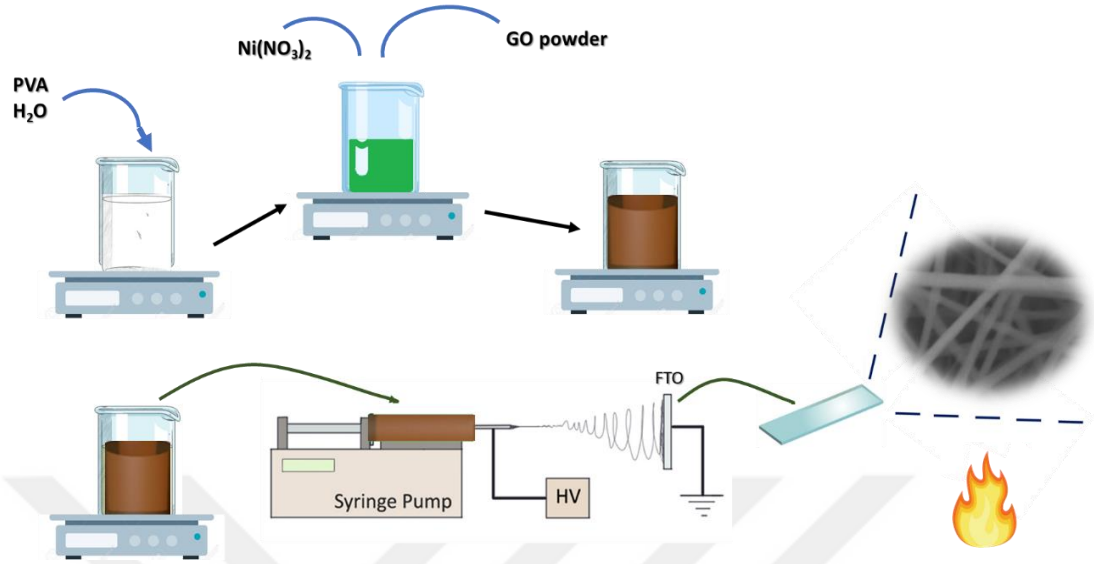

Figure 3.9. The synthesis procedure of rGO/Ni/NiO nanofibers

The optimum synthesis method can be summarized step by step as follows:

- PVA is dissolved in deionized water.
- The GO dispersion and the Ni salt are added to the PVA solution.
- The precursor is loaded into the syringe and directly spun onto the FTO surface using a monoaxial electrospinning device.
- Fibers coated on the FTO surface are calcined at 340 °C in dry air for one hour.

3.2.5 Synthesis of rGO_x/Ni/NiO nanofibers

For preparing the electrospinning precursor, 2.50 g of PVA solution (10% by weight of PVA) was stirred for 6 hours. The FTO substrate was covered with aluminum foil to set the electrode area to 1 cm × 1 cm. GO powder was dispersed by sonication in 0.5 mL of water for 30 minutes at a ratio of 1:5, 1:8, 1:10, 1:12, and 1:15 by weight compared to Ni salt and added to the PVA/$Ni(NO_3)_2.6H_2O$ solution. The solution was filled into a 5 mL plastic syringe.

In order to obtain equal nanofibers, the high potential applied to the system, the distance between the tip and the collector, and the flow rate of the solution must be in a "balance".

In addition, the ideal ratio of the amount of polymer in the solution, the solvent and the metal to be spun should be determined. In our experiments, determining these parameters was extra challenging because all solutions had to be spun with the same parameters in order to obtain equal amounts of rGO, Ni/NiO and rGO/Ni/NiO fibers on the FTO surface. After many trial and error attempts, the fibers were spinned directly on the FTO surface by applying a voltage of 12 kV between the syringe tip and the FTO, keeping the tip at a distance of 17 cm from FTO. Throughout this experiment, the solution had a flow rate of 0.4 mL/h for 1 hour. Nanofibers consisting of PVA/GO, PVA/$Ni(NO_3)_2.6H_2O$, and PVA/GO/$Ni(NO_3)_2.6H_2O$ were left in a vacuum chamber at 60 °C for 1 hour. Then, as-spun fibers were calcined at 340 °C for 1 hour at a heating rate of 8 °C min^{-1} in an air atmosphere to obtain rGO/Ni/NiO heterostructures.

Thermogravimetric analysis (TGA) method was used to investigate the thermal degradation of nanofibers. Nanofibers containing only PVA were synthesized and these fibers were exposed to heat from room temperature to 600 °C at a rate of 8 ^oC min^{-1} under dry air. As seen in Figure 3.10, inflections were observed at 300 °C and 405 °C, corresponding to the decomposition of the side chain and main chain of PVA, respectively [96]. Up to 9% weight loss was observed for the PVA nanofibers when the temperature reached 100 °C and approximately 70% from 200 to 300 °C. Based on the TGA analysis, it was decided that PVA could be eliminated by using a temperature value of 300 ^oC and above. As a result of the electrodes calcined many times using different temperatures, it was decided that the optimum calcination temperature for our sample was 340 ^oC.

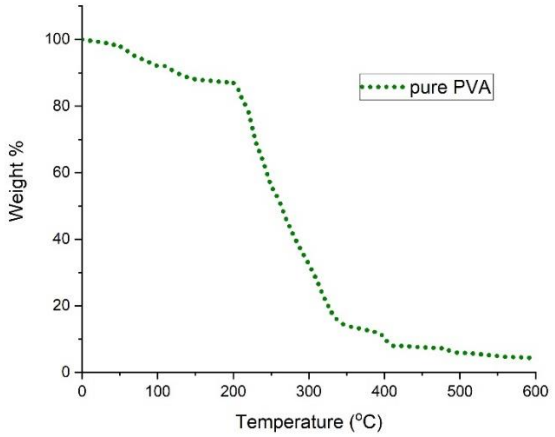

Figure 3.10 Thermogravimetric analysis of pure PVA nanofibers

The electrospun fibers were calcined at 340 °C for 1 hour at a heating rate of 8 °C min^{-1} in dry air to obtain rGO_x/Ni/NiO nanofibers. By calcination procedure, PVA was eliminated from nanofibers and rGO/Ni/NiO nanofibers were obtained. The solutions obtained with 1:5, 1:8, 1:10, 1:12 and 1:15 ratios were labeled as $rGO_{0.2}$/Ni/NiO, $rGO_{0.125}$/Ni/NiO, $rGO_{0.1}$/Ni/NiO, $rGO_{0.083}$/Ni/NiO and $rGO_{0.067}$/Ni/NiO for after calcination, respectively (Table 3.1).

Table 3.1. GO powder at a ratio of 1:5, 1:8, 1:10, 1:12, 1:15 by weight compared to Ni salt.

GO:Ni salt	Labels (before calcination)	Labels (after calcination)
1:5	PVA/$GO_{0.2}$/$Ni(NO_3)_2.6H_2O$	$rGO_{0.2}$/Ni/NiO
1:8	PVA/$GO_{0.125}$/ $Ni(NO_3)_2.6H_2O$	$rGO_{0.125}$/Ni/NiO
1:10	PVA/$GO_{0.1}$/ $Ni(NO_3)_2.6H_2O$	$rGO_{0.1}$/Ni/NiO
1:12	PVA/$GO_{0.083}$/ $Ni(NO_3)_2.6H_2O$	$rGO_{0.083}$/Ni/NiO
1:15	PVA/$GO_{0.067}$/ $Ni(NO_3)_2.6H_2O$	$rGO_{0.067}$/Ni/NiO

3.2.6 Characterization of rGO_x/Ni/NiO heterostructured NFs

SEM images of PVA/$GO_{0.125}$/$Ni(NO_3)_2.6H_2O$, PVA/$GO_{0.1}$/$Ni(NO_3)_2.6H_2O$ and PVA/$GO_{0.083}$/$Ni(NO_3)_2.6H_2O$ showing the ratio of GO to Ni examined (Figure 3.11). Samples with a concentration of 1:10 and 1:12 had a fibrous structure. However, when the ratio of GO to Ni salt was greater than 1:10, instability occurred during the spinning of the precursor. Bead-strand fibers were observed as a result of this instability for PVA/$GO_{0.125}$/$Ni(NO_3)_2.6H_2O$ (Figure 3.11a). Excessive amounts of GO may have resulted in the appearance of beads, which may be due to aggregation of GO via π-π interactions [97].

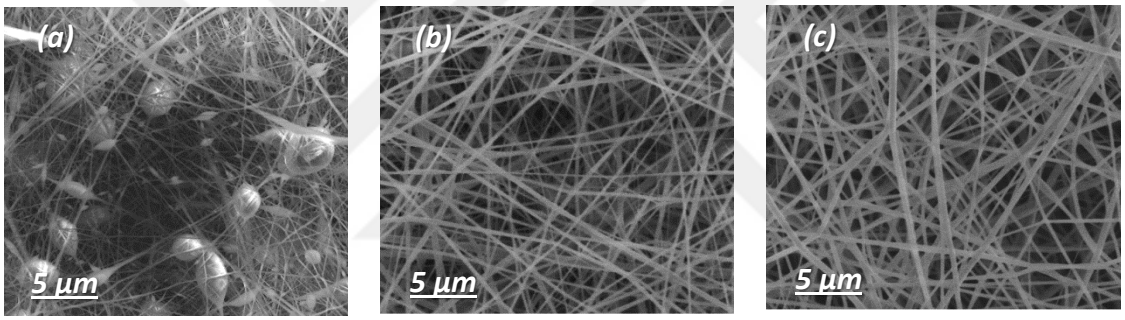

Figure 3.11. SEM images of (a-c) electrospun PVA/$GO_{0.125}$/$Ni(NO_3)_2.6H_2O$, PVA/$GO_{0.1}$/$Ni(NO_3)_2.6H_2O$, and PVA/$GO_{0.083}$/$Ni(NO_3)_2.6H_2O$

3.2.7 $rGO_{0.1}$/Ni/NiO heterostructured NFs as optimum sample

Due to the beading observed in the SEM images of PVA/$GO_{0.2}$/$Ni(NO_3)_2.6H_2O$ and PVA/$GO_{0.125}$/$Ni(NO_3)_2.6H_2O$ fibers, the electrochemical performances of $rGO_{0.1}$/Ni/NiO, $rGO_{0.083}$/Ni/NiO, and $rGO_{0.067}$/Ni/NiO nanofibers obtained as a result of calcination of PVA/$GO_{0.1}$/$Ni(NO_3)_2.6H_2O$, PVA/$GO_{0.083}$/$Ni(NO_3)_2.6H_2O$, and PVA/$GO_{0.067}$/$Ni(NO_3)_2.6H_2O$, at 340 °C for 1 hour were tested in 1 M KOH by lineer sweep voltammetry (LSV) technique. By comparing the electrochemical performances, $rGO_{0.1}$/Ni/NiO nanofibers were decided as the optimum catalyst. A detailed discussion of the results is provided in Section 3.3.2.

3.2.7.1 Morphological studies

Low and high magnification SEM images of PVA/$GO_{0.1}$/$Ni(NO_3)_2.6H_2O$ (Figure 3.12a-d) and $rGO_{0.1}$/Ni/NiO NFs (Figure 3.12e-h) calcined in dry air for one hour are shown in Figure 3.12. After annealing, it was observed that the NF morphologies changed significantly, the surface roughness increased and the NFs turned into a nanofiber-like morphology. Due to the degradation of PVA during this process, the mean diameter of the NFs decreased.

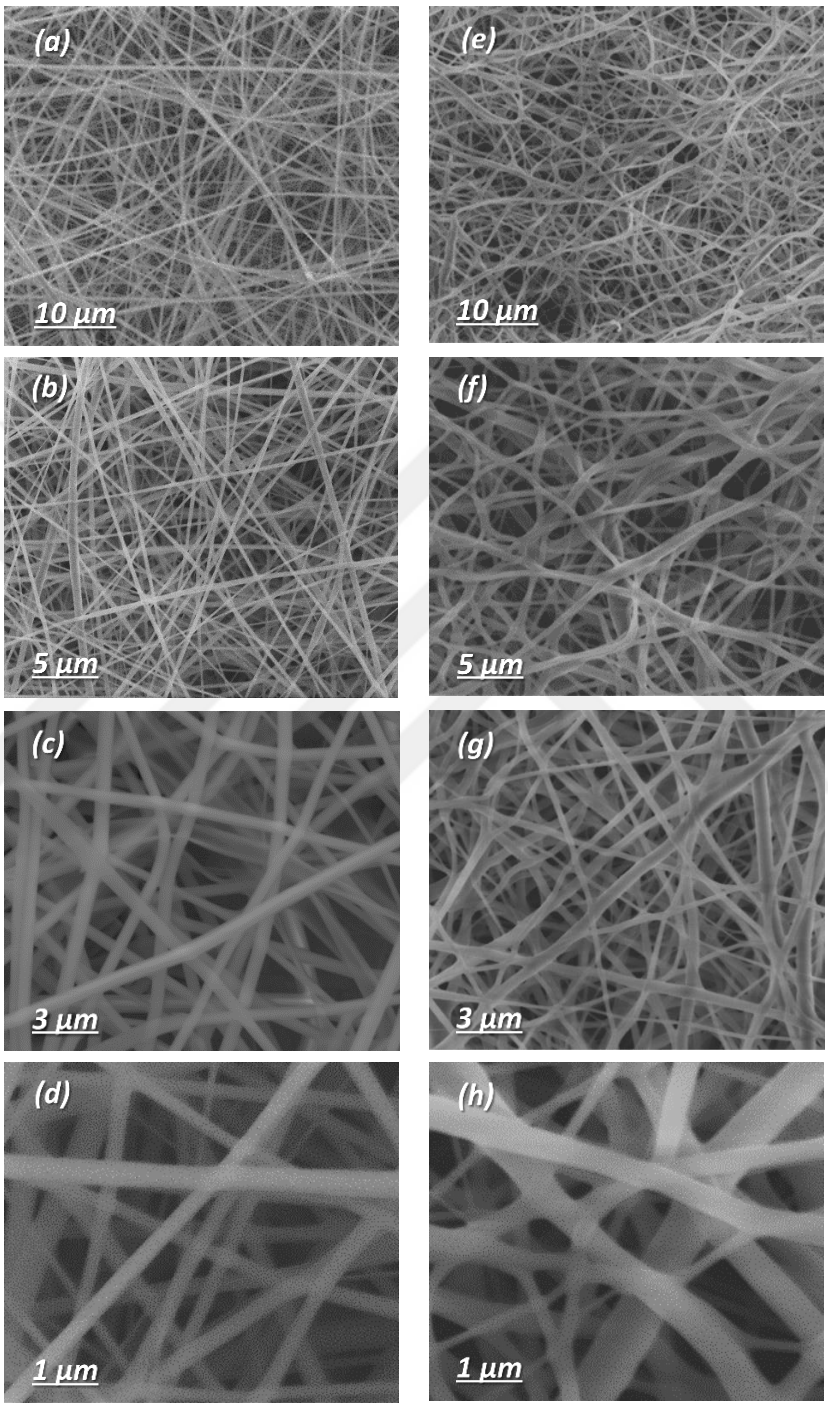

Figure 3.12 Low and high magnification SEM images of (a-d) electrospun PVA/$GO_{0.1}$/$Ni(NO_3)_2.6H_2O$ NFs prior to calcination, (e-h) $rGO_{0.1}$/Ni/NiO NFs after calcination.

SEM images of Ni/NiO and rGO NFs before and after calcination are shown in Figure 3.13 and Figure 3.14, respectively. Polymer solutions with good electrical conductivity are used to produce fibers by the electrospinning technique. While the metal salts used increase the conductivity, the conductivity of the precursor prepared for obtaining rGO/Ni/NiO fibers decreases with the addition of GO. As mentioned earlier, reduction is essential to increase the conductivity of GO. As a result of adding a dispersion of low electrical conductivity GO to the precursor, it became difficult to spin under the same electrospinning parameters, resulting in a smaller diameter and less uniform fiber coating on the FTO substrate.

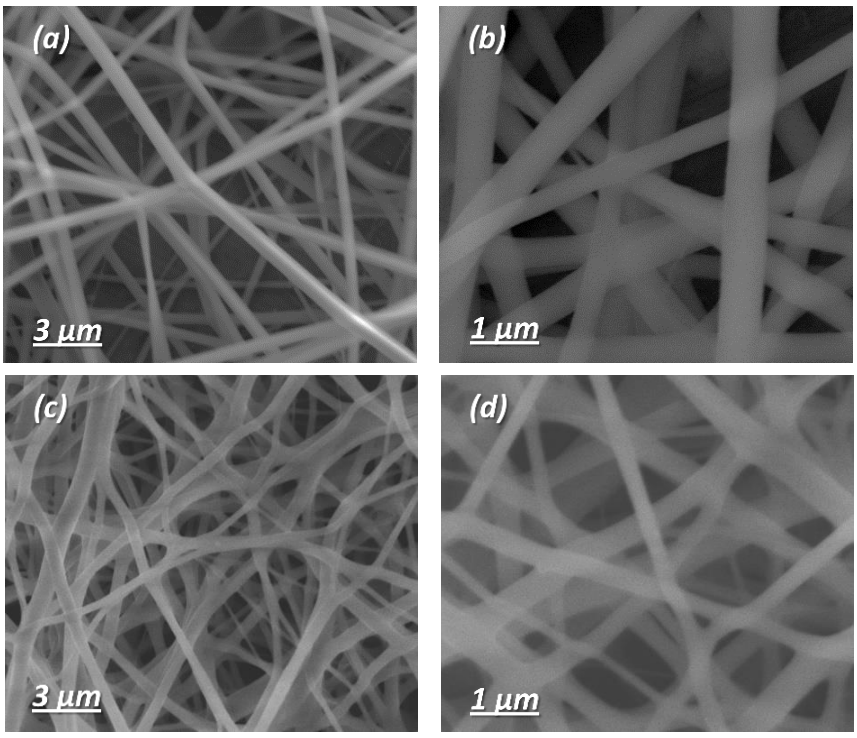

Figure 3.13 Low and high magnification SEM images of (a-b) electrospun PVA/$Ni(NO_3)_2.6H_2O$ NFs prior to calcination, (c-d) Ni/NiO NFs after calcination.

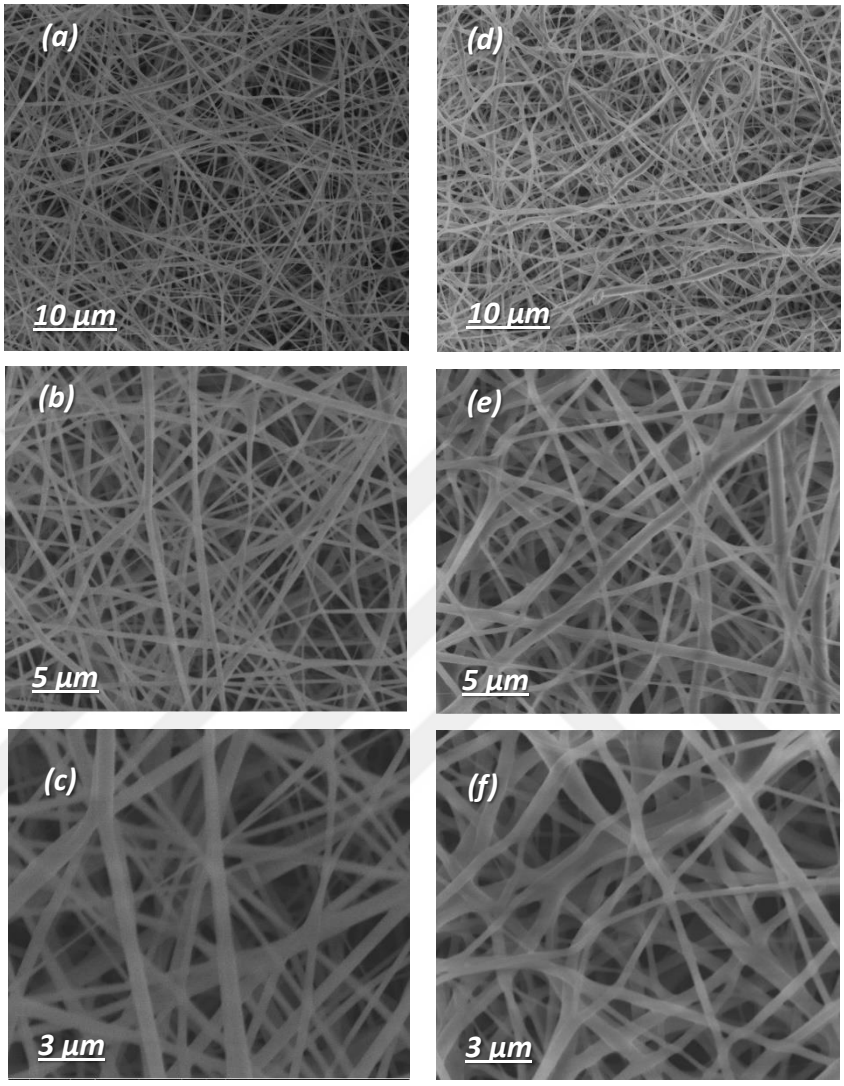

Figure 3.14. SEM images of (a-c) electrospun PVA/GO nanofibers prior to calcination, (d-f) electrospun rGO nanofibers after calcination.

SEM-EDX analyzes of PVA/$Ni(NO_3)_2.6H_2O$, and Ni/NiO NFs are given in Figure 3.15. While the atomic percentages of C, O and Ni for PVA/$Ni(NO_3)_2.6H_2O$ before calcination were 64.32, 34.68 and 1.00, respectively (Figure 3.15a), in the EDX analysis of Ni/NiO fibers after thermal treatment of PVA/$Ni(NO_3)_2.6H_2O$ NFs, a small percentage of C was determined (Figure 3.15b). This confirms the degradation of PVA. The relatively small percentage of C atoms observed (3.57%) may be due to the carbon tape used to prepare

the sample for SEM analysis. After calcination, the atomic percentage of Ni increased to 36.68%.

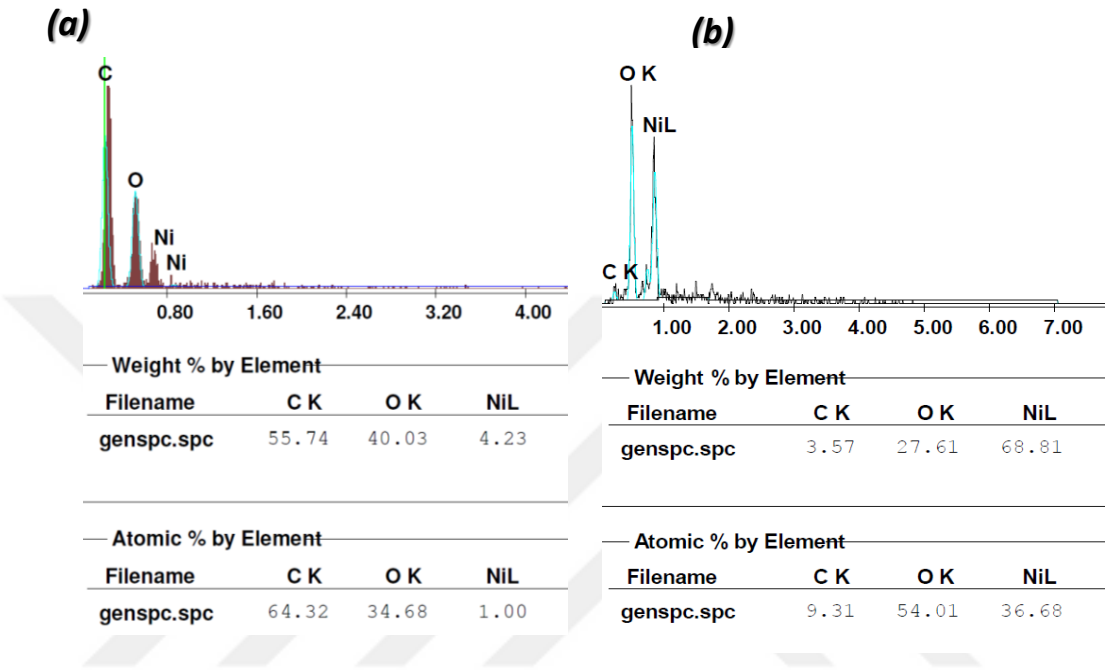

Figure 3.15 SEM-EDX analysis of (a) PVA/$Ni(NO_3)_2.6H_2O$, and (b) Ni/NiO NFs

HRTEM images of the as-spun fibers are given in Figure 3.16. In the elemental mapping of $rGO_{0.1}$/Ni/NiO fibers after calcination, red, orange and blue colorings were made for Ni, C and O, respectively (Figure 3.16e-h). By looking at the mapping, it can be deduced that the elements have an even distribution in the nanofiber. The SAED pattern of the fibers is given in Figure 3.16d. The bright dots in the image point to Ni.

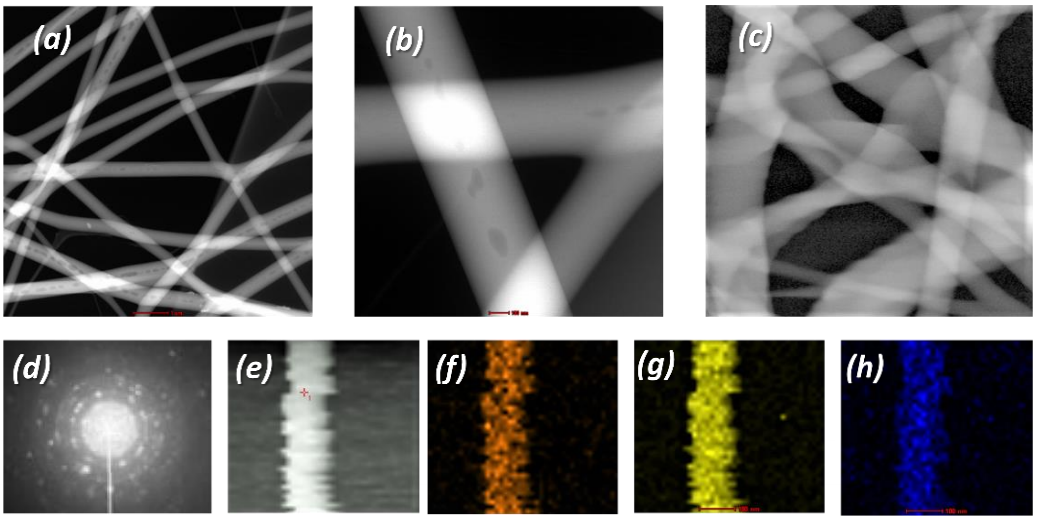

Figure 3.16 (a, b) TEM images of electrospun PVA/$GO_{0.1}$/Ni$(NO_3)_2$.$6H_2O$ nanofibers. (c) TEM image of electrospun r$GO_{0.1}$/Ni/NiO nanofibers. (d) SAED pattern. (d) TEM-EDX-based elemental mapping.

3.2.7.2 X-ray diffraction spectroscopy (XRD)

The crystal structures of the samples were investigated using X-ray diffraction analysis. Figures 3.17a-c represent the XRD pattern of PVA/$GO_{0.1}$/Ni$(NO_3)_2$.$6H_2O$ Ni/NiO and r$GO_{0.1}$/Ni/NiO NFs, respectively. In the XRD spectrum shown in Figure 3.17a for PVA/$GO_{0.1}$/Ni$(NO_3)_2$.$6H_2O$, a characteristic sharp peak was observed for PVA at 21° and a diffraction peak (001) appeared at 12.5° for the GO layers [98]. Figure 3.17c shows the XRD pattern after calcination of r$GO_{0.1}$/Ni/NiO NFs. As a result of thermal reduction, the (001) peak disappeared, and the change in this peak characteristic for GO indicates a reduction in GO in the fiber. Based on the XRD pattern, we see that the reduction process was successfully completed at 340 °C. It has also been confirmed that 340 °C is a sufficient temperature for the degradation of PVA. The absence of a peak at 21° indicating the presence of PVA after calcination confirmed the elimination of PVA. The peaks seen at 37.2°, 43.2° and 62.8° in the r$GO_{0.1}$/Ni/NiO XRD model correspond to the (111), (200) and (220) diffraction planes of face-centered cubic (FCC) NiO, respectively, indicate that NiO has high crystallinity [99]. The two diffraction peaks at 44.5° and 51.9°

in the XRD model correspond to the Ni(111) and Ni(200) diffraction planes of the FCC Ni structure, respectively [100]. Moreover, the XRD pattern of Ni/NiO NFs shown in Figure 3.17b is consistent with $rGO_{0.1}$/Ni/NiO NFs with characteristic peaks for Ni and NiO. It is understood that PVA was successfully eliminated during the calcination for the Ni/NiO sample as well.

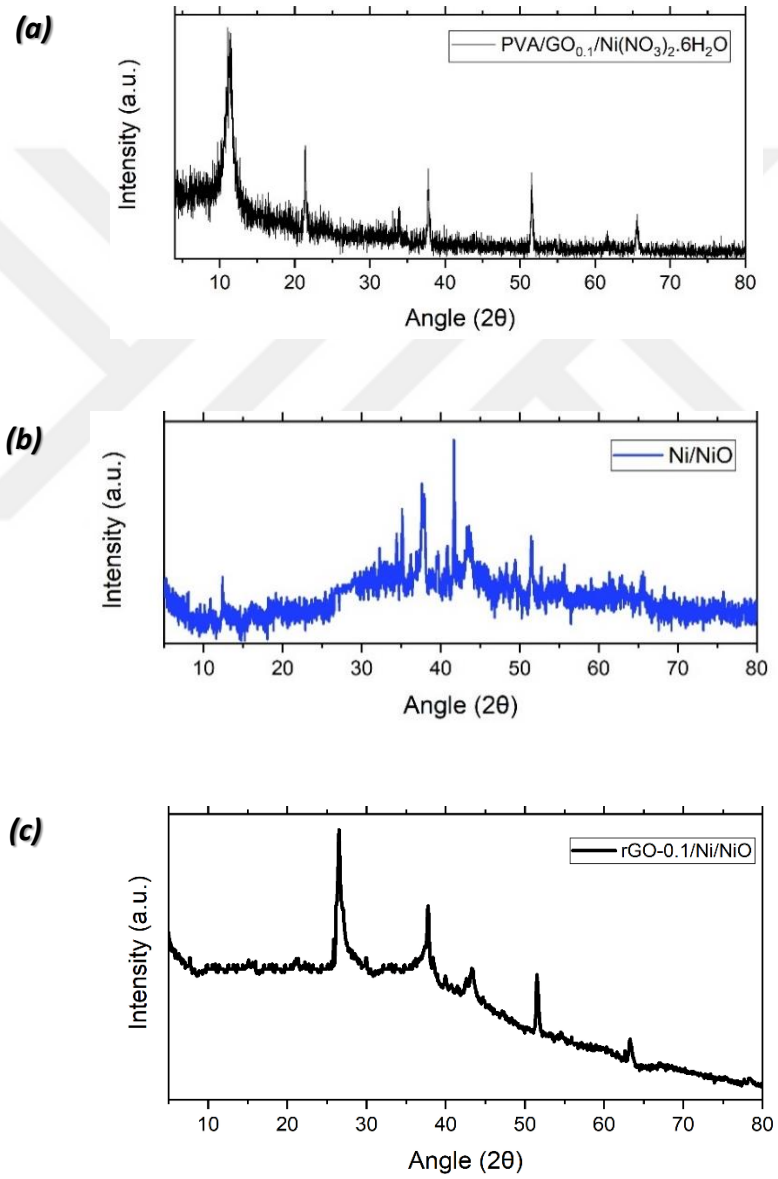

Figure 3.17. X-ray diffraction pattern of (a) $PVA/GO_{0.1}/Ni(NO_3)_2.6H_2O$, (b) Ni/NiO and (c) $rGO_{0.1}$/Ni/NiO NFs.

3.2.7.3 Raman spectroscopy

Figure 3.18a-c shows the Raman spectrum of rGO, PVA/$GO_{0.1}$/$Ni(NO_3)_2.6H_2O$ and $rGO_{0.1}$/Ni/NiO NFs, respectively. GO and rGO exhibit prominent D and G bands [101]. The PVA/$GO_{0.1}$/$Ni(NO_3)_2.6H_2O$ spectrum showed peaks at 1350 cm^{-1} and 1589 cm^{-1}, indicating the D-band and G-band, respectively. The D-band is attributed to the respiration mode of the sp^2 carbon. In the rGO obtained after reduction, there are new sp^2 carbon atoms smaller in size than the sp carbon atoms found in GO. Therefore, the average crystallite size of sp^2 domains showed a reduction in rGO compared to GO [102]. This explains the observed increase in Raman D-band for both rGO and $rGO_{0.1}$/Ni/NiO nanofibers. Besides, the G-band indicates optical mode vibration of two adjacent carbon atoms [103]. After thermal reduction, the G-band appears to shift to a lower wave number as a result of the increase in the number of sp^2 carbon atoms. Raman spectra of $rGO_{0.1}$/Ni/NiO NFs showed a distinct G-band (approx. 1580 cm^{-1}) and D-band (approx. 1360 cm^{-1}) peak, similar to pure rGO NFs. Also, Figure 5 shows this peak shift in the G-band as a result of the reduction process more closely. As a result, the thermal reduction of GO at 340 °C was confirmed by examining the Raman spectra of the electrodes.

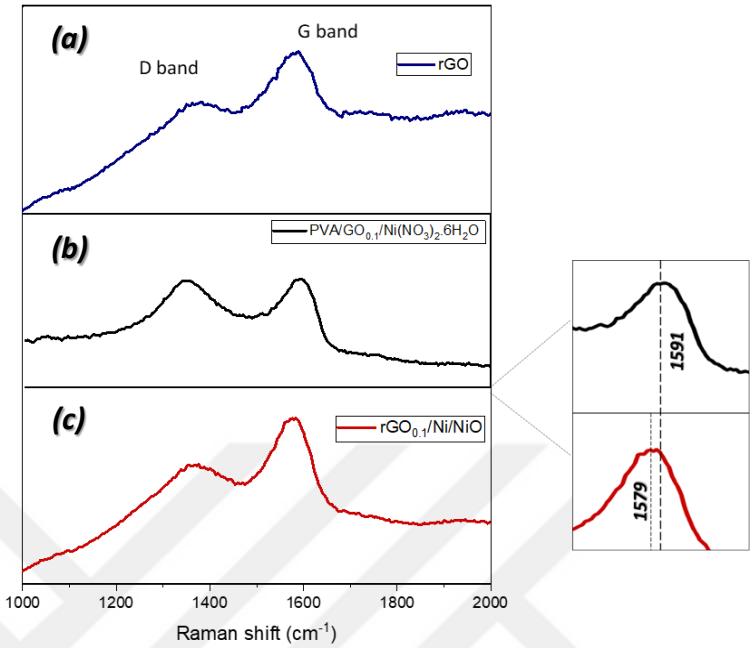

Figure 3.18. Raman spectra of (a) rGO (b) $PVA/GO_{0.1}/Ni(NO_3)_2.6H_2O$ and c) $rGO_{0.1}/Ni/NiO$ NFs.

3.2.7.4 X-ray photoelectron spectroscopy (XPS)

XPS was used to evaluate the chemical valence state of $PVA/GO_{0.1}/Ni(NO_3)_2.6H_2O$ and $rGO_{0.1}/Ni/NiO$ fibers. As shown in Figure 3.19b, after calcining the nanofibers, the peaks of the oxygen-containing groups appear to be significantly reduced. Thus, it has been demonstrated that oxygen-containing groups are effectively eliminated as a result of removal of PVA from the sample and thermal reduction. Figure 3.19c shows the Ni 2p spectrum for $PVA/GO_{0.1}/Ni(NO_3)_2.6H_2O$ NFs. For this sample, two peaks are seen around 856.7 eV and 874.4 eV, and these peaks are assigned to Ni $2p_{3/2}$ and Ni $2p_{1/2}$, respectively. They are compatible with Ni^{2+} in NiO. Also, two satellite peaks were observed at 862.1 eV and 880.7 eV. The Ni 2p spectrum belonging to the $rGO_{0.1}/Ni/NiO$ heterostructure obtained after calcination is given in Figure 3.19d. For $rGO_{0.1}/Ni/NiO$, four pairs of peaks are seen in the Ni 2p spectrum. The peak pair found at 852.43 eV and 870.4 eV is attributed to NiO, metallic Ni. Two residual peaks were observed at 855.63 eV and 873.47 eV, indicating the presence of Ni_2O_3 at the electrode [104]. Ni_2O_3 is

formed from oxygen-enriched NiO, which can result from the combustion of carbon during the calcination process [105].

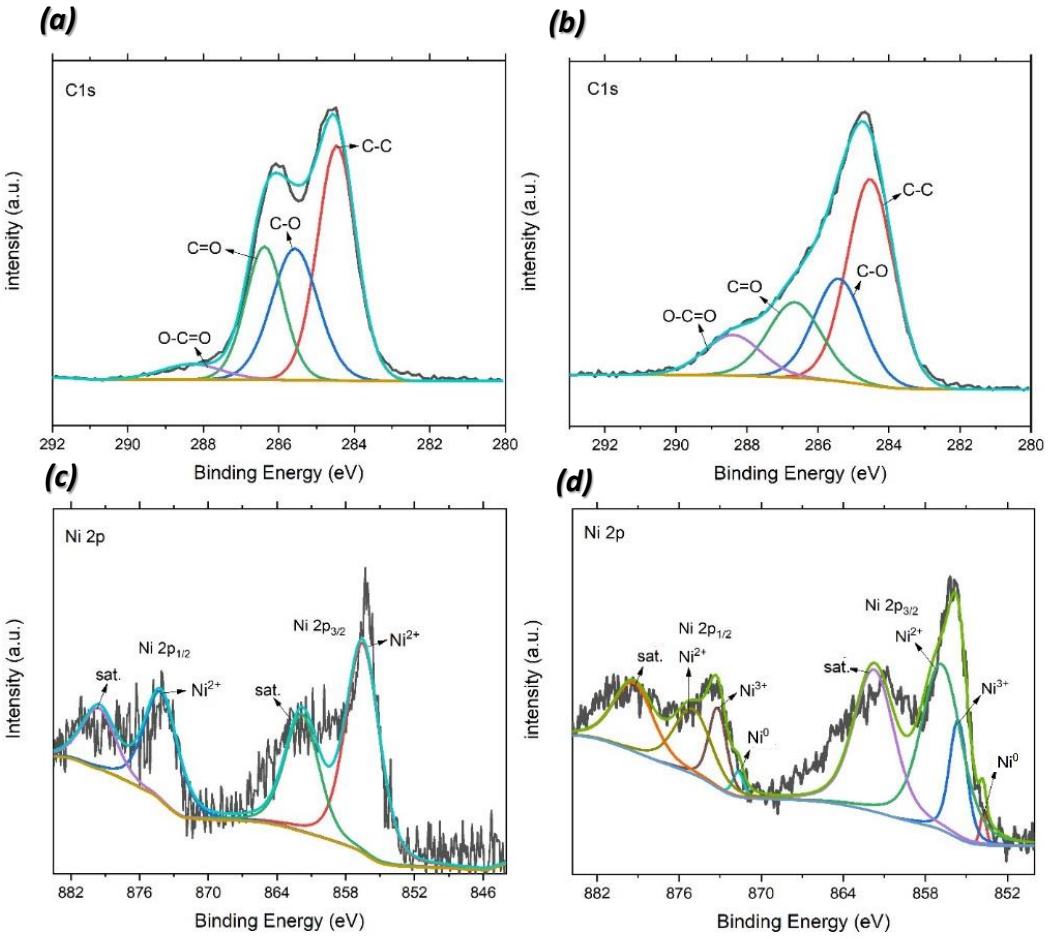

Figure 3.19. High resolution XPS spectra of (a) C 1s and (b) Ni 2p spectra of as-spun PVA/$GO_{0.1}$/$Ni(NO_3)_2.6H_2O$ NFs and (c) C 1s and (d) Ni 2p spectra of r$GO_{0.1}$/Ni/NiO NFs.

3.3 Electrochemical analysis

All electrochemical measurements were performed at room temperature using the SP-300 (BioLogic, France) potentiostat with a conventional three-electrode cell configuration. Silver/Silver chloride (Ag/AgCl/KCl (sat)) and Pt spiral wire were used as reference electrode and counter electrode, respectively. The electrodes obtained as a result of coating the nanofibers on the FTO surface were used as working electrodes. FTOs were thoroughly cleaned by washing and sonicated in deionized water followed by isopropanol for 15 minutes each. The FTO surfaces were then activated by heat exposure in the oven at 350°C for 1 hour. The catalysts in fiber form were electrospinned onto a 1x1 cm^2 portion of the FTO. In addition, to obtain rGO surfaces, the GO dispersion was coated on the FTO surface using the drop casting method and left to dry at air temperature overnight. Electrolytes were deaerated for half an hour using Argon gas before each experiment to remove unwanted dissolved gases from the electrolyte. Potentials are calculated using Equation 3-1 and reported against the reversible hydrogen electrode (RHE);

$$E\ (\text{vs. RHE}) = E_{(Ag/AgCl/KCl\ (sat))} + 0.059*pH + E^0_{(Ag/AgCl/KCl\ (sat))} \qquad \text{(Equation 3-1)}$$

E represents the potential of the electrode with respect to RHE, $E_{(Ag/AgCl/KCl\ (sat))}$ indicates the potential measured by the potentiostat, and $E^0_{(Ag/AgCl/KCl\ (sat))}$ indicates the standard potential, i.e. 0.197 V.

3.3.1 Electrocatalytic behavior of rGO/Ni/NiO in alkaline electrolyte

Electrolytes containing 0.1 M and 1 M KOH were used to observe the electrochemical behavior of the rGO/Ni/NiO catalyst. The LSV curve showing the potential versus current density of rGO/Ni/NiO in alkaline media at two different concentrations is given in Figure 3.20.

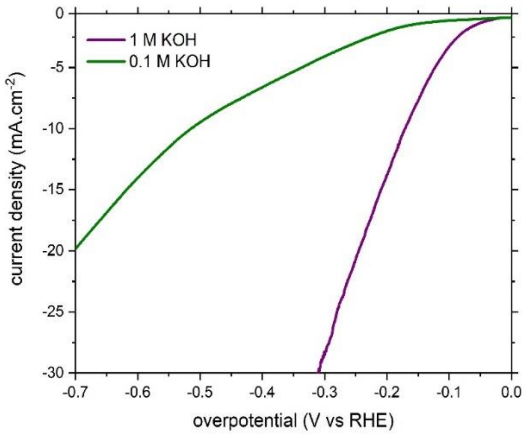

Figure 3.20 Polarization curves of rGO/Ni/NiO in different solution media.

It is seen that the rGO/Ni/NiO catalyst exhibits a significantly smaller overpotential at 1 M KOH at the same current density (@10 mA cm^{-2}) when the KOH concentration in the electrolyte, i.e. the ions required for HER, increases in solution compared to 0.1 M KOH. Therefore, all experiments were carried out using an electrolyte containing 1 M KOH. The same significant difference is seen in the onset potentials of the catalyst in these two different alkaline media.

3.3.2 Electrocatalytic performance of rGO_x/Ni/NiO

The HER performances of $rGO_{0.1}$/Ni/NiO, $rGO_{0.083}$/Ni/NiO and $rGO_{0.067}$/Ni/NiO nanofibers were investigated by LSV measurement with a scan rate of 10 mV s^{-1}. As shown in Figure 3.21, $rGO_{0.1}$/Ni/NiO NFs have the lowest overpotential of -212 mV at 10 mA cm^{-2} compared to $rGO_{0.083}$/Ni/NiO and $rGO_{0.067}$/Ni/NiO NFs. It is understood that the increase in the amount of rGO compared to the amount of Ni/NiO in the fibers increases the HER activity. However, when preparing precursors for nanofibers, the ratio of GO to Ni salt greater than 1:10 caused instability during electrospinning. As the amount of GO in the solution increased, the electrical conductivity decreased, resulting in a higher voltage applied to the system for spinning. As a result of the increase in the charge density on the jet, deformation occurs and as a result, ultra-thin and different fiber diameters are obtained. This is due to the excessive charge density causing unstable

motion of the jet [106]. This instability causes the fibers to be randomly oriented. Therefore, $rGO_{0.1}$/Ni/NiO was chosen as the optimal catalyst for HER.

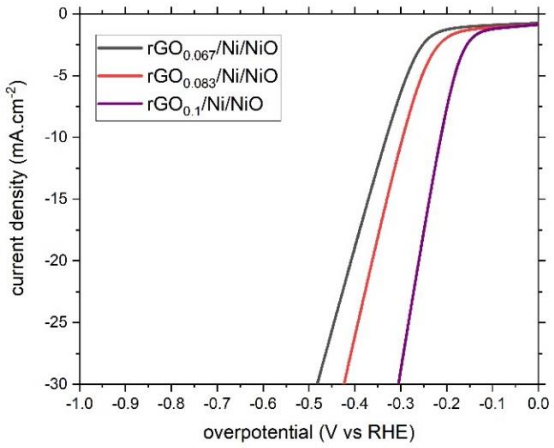

Figure 3.21 LSV curves of $rGO_{0.1}$/Ni/NiO, $rGO_{0.083}$/Ni/NiO and $rGO_{0.067}$/Ni/NiO in 1 M KOH.

3.3.3 Electrocatalytic performance of the optimum sample: $rGO_{0.1}$/Ni/NiO

HER activities of Ni/NiO, rGO and $rGO_{0.1}$/Ni/NiO electrocatalysts were examined in LSV. The performance of these catalysts was compared with that of 10% Pt/C, which is considered as a state-of-the-art electrocatalyst (Figure 3.22a).

While rGO nanofibers could not exhibit a significant HER current density before -0.3 V, $rGO_{0.1}$/Ni/NiO showed the lowest onset potential compared to rGO and Ni/NiO electrocatalysts at 180 mV. For $rGO_{0.1}$/Ni/NiO, Ni/NiO and rGO catalysts, a current density of 10 mA cm^{-2} was obtained at -212 mV, -260 mV and -505 mV overpotentials, respectively. The catalytic activity of the electrocatalysts for HER increased in the order of rGO < Ni/NiO < $rGO_{0.1}$/Ni/NiO.

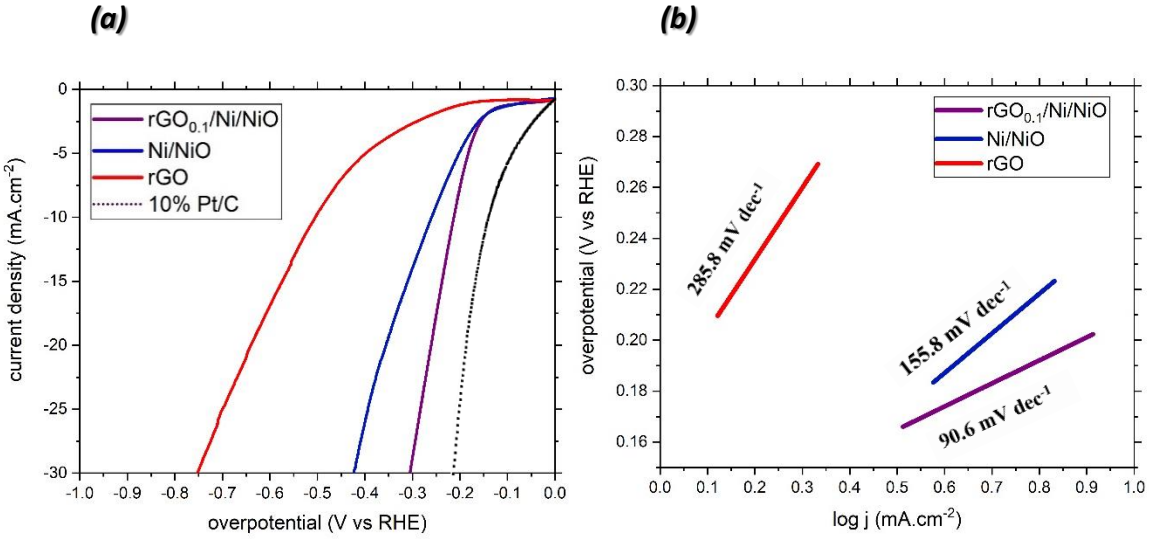

Figure 3.22 (a) LSV polarization curves of rGO, Ni/NiO and $rGO_{0.1}$/Ni/NiO at 10 mV s^{-1} in 1 M KOH, (b) corresponding Tafel plots in linear region.

After the water molecule is adsorbed on the catalyst surface, it dissociates into H^+ and OH^- ions on the surface. At this point, NiO plays an important role in breaking the HO−H bonds. Thanks to the high H binding energy of Ni metal, H^+ ions are adsorbed to the surface, while OH- ions are desorbed by NiO. This role of Ni is also essential because new atoms can be adsorbed onto the catalyst surface. The OH^- ion has a desire to bind to positively charged Ni species. Considering the Ni/NiO interface, OH^- tends to bind to the NiO site since the d orbitals of Ni^{2+} are more vacant. For all its advantages, NiO alone is a poor catalyst for HER. Because although it has been reported as a catalyst with high electrocatalytic activity for OER, it does not have enough adsorption sites for H^+. The important point of NiO in the Ni/NiO heterostructure is that by adsorbing OH^- species, it increases the adsorption probability of the H atoms of Ni. In this way, it provides better catalytic activity [107-108].

To further characterize the samples, the Tafel slope was obtained from the LSV polarization plots. The Tafel chart provides important information about the rate-limiting digit of HER. Tafel slope values of 120, 40 and 30 mV/dec are classified as the discharge (Volmer step), electrochemical desorption (Heyrovsky step) and recombination (Tafel step) reactions as rate determination steps (RDS) for HER, respectively. Tafel, Volmer

and Heyrovsky steps in alkaline medium (Table 3.2). A lower Tafel slope means faster kinetics for HER. By analyzing how much potential should be applied to the system for a given current density window, it is desirable to use the catalyst that needs the least overpotential. This means a lower Tafel slope.

Table 3.2. Mechanism of HER in acidic and alkaline electrolytes

Acidic electrolyte	**Alkaline electrolyte**
$2H^+ + 2e^- \rightarrow H_2$	$2H_2O + 2e^- \rightarrow H_2 + 2OH^-$
➢ Volmer	➢ Volmer–water dissociation
$H^+ + e^- \rightarrow H_{ads}$	$2H_2O + 2e^- \rightarrow 2H_{ads} + 2OH^-$
➢ Tafel	➢ Tafel
$2H_{ads} \rightarrow H_2$	$2H_{ads} \rightarrow H_2$
➢ Heyrovsky	➢ Heyrovsky
$H^+ + H_{ads} + e^- \rightarrow H_2$	$H_2O + H_{ads} + e^- \rightarrow H_2 + OH^-$

Figure 3.22b shows the Tafel plot of rGO, Ni/NiO and $rGO_{0.1}$/Ni/NiO NFs. The Tafel slopes of rGO, Ni/NiO and $rGO_{0.1}$/Ni/NiO catalysts were found to be 285.8 mV dec^{-1}, 155.8 mV dec^{-1} and 90.6 mV dec^{-1}, respectively. Based on this result, it can be deduced that the $rGO_{0.1}$/Ni/NiO heterostructure has the fastest kinetics. From the rate determination steps for HER, it is understood that all electrocatalysts have Volmer-Heyrovsky mechanism. The comparison of Tafel slope of the various catalysts is listed in Table 3.3.

Table 3.3. A comparison for HER performances of Ni-based or carbon-supported catalysts.

Catalyst	***Electrolyte***	***Tafel slope (mV dec^{-1})***	***Ref. No.***
C@NiO/Ni	1 M KOH	152	[82]
Ni-Co on carbon fiber paper	1 M KOH	177.78	[109]
Fe-Ni-Graphene	6 M NaOH	125	[110]
Ni-CNTs	1 M NaOH	135	[111]
Ni/NiO-CNTs	1 M KOH	67	[112]
rGO/Ni/NiO NFs	1 M KOH	90.6	This work

Total electrode activity is determined by the two main factors, the intrinsic activity of the electrocatalyst and the number of active sites (or electrochemical surface area, ECSA).

Cyclic voltammetry (CV) scans were used to obtain the C_{dl} values of $rGO_{0.1}$/Ni/NiO and Ni/NiO electrocatalysts. CV experiments at different scan rates from 100 mV to 200 mV (100 mV, 125 mV, 150 mV, 175 mV and 200 mV) were repeated at 1 M KOH (Figure 3.23a-b). CV scans were recorded in a non-Faradic region (from -0.12 V to -0.20 V to RHE). The results showed that $rGO_{0.1}$/Ni/NiO has a larger ECSA value, exhibiting a larger C_{dl} value of 163 µF cm^{-2} compared to Ni/NiO with a C_{dl} value of 80 µF cm^{-2} (Figure 3.23d). The greater C_{dl} value of the $rGO_{0.1}$/Ni/NiO catalyst compared to Ni/NiO can be attributed to the high specific surface area of rGO.

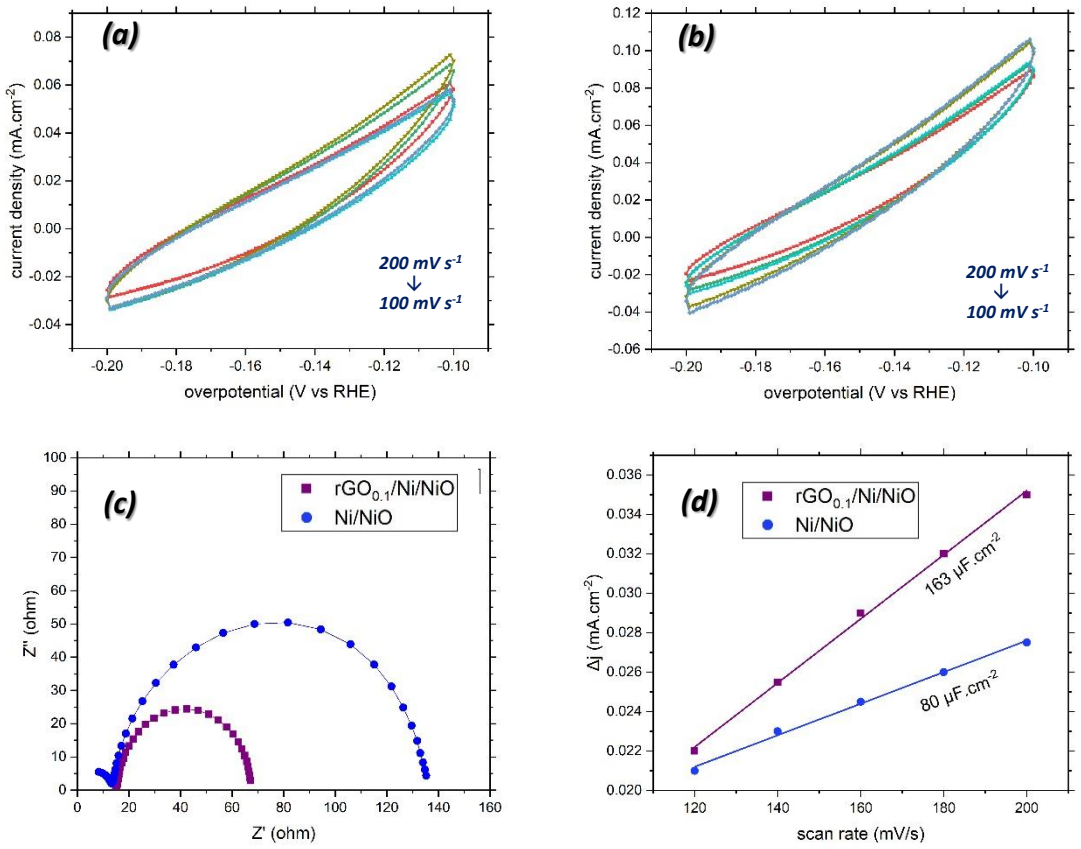

Figure 3.23 (a) CVs of Ni/NiO at different scan rates. (b) CVs of $rGO_{0.1}$/Ni/NiO at different scan rates. (c) Nyquist plots measured at −0.3 V vs RHE for Ni/NiO and $rGO_{0.1}$/Ni/NiO catalysts. (d) scan rate dependence of the current densities of Ni/NiO and $rGO_{0.1}$/Ni/NiO NFs.

Figure 3.23c shows electrochemical impedance spectroscopies (EIS) of Ni/NiO and $rGO_{0.1}$/Ni/NiO electrocatalysts performed to examine HER kinetics. Impedance spectroscopy experiments were performed at 1 M KOH versus −0.3 V at RHE for the frequency range 0.1 Hz to 100 kHz. Based on the Nyquist plot, $rGO_{0.1}$/Ni/NiO and Ni/NiO heterostructures were found to exhibit charge transfer resistance (Rct) of 52 Ω and 123 Ω, respectively. It was deduced that rGO/Ni/NiO with smaller Rct value exhibited faster charge transfer kinetics. This result shows that the reduced graphene

oxide nanostructure with high electrical conductivity in $rGO_{0.1}$/Ni/NiO NFs provides faster electron transfer to the catalyst. The electrochemical parameters of $rGO_{0.1}$/Ni/NiO, Ni/NiO and rGO NFs have been summarized in Table 3.4.

Table 3.4 Electrochemical parameters of rGO/Ni/NiO, Ni/NiO and rGO NFs.

Sample	**Onset Potential (mV)**	**η @10 mA cm^{-2} (mV)**	**Tafel slope (mV dec^{-1})**	**R_{ct} (Ω)**
Ni/NiO	-165	-260	155.8	123
rGO/Ni/NiO	-160	-212	90.6	52
rGO	-489	-505	285.8	---

3.3.4 The effect of Intrinsic and extrinsic activities on catalysts

Heterostructured nanofibers containing reduced graphene oxide were fabricated to improve the catalytic activity of our catalyst for HER. By using rGO, it is aimed to provide more surface area to the catalyst and thus to increase the number of active sites. Based on the same logic, it was desired to improve the number of active sites by synthesizing the catalyst in nanofiber form using the electrospinning method. This allows the extrinsic catalytic activity of the catalyst to improve. The design of heterostructured catalysts can create new catalytic domains by improving charge transfer kinetics at the interfaces. By enabling Ni/NiO to facilitate the decomposition of water, the intrinsic catalytic activity of the catalyst is improved. For this purpose, LSV curves of rGO in nanolayer and nanofiber form were compared (Figure 3.24).

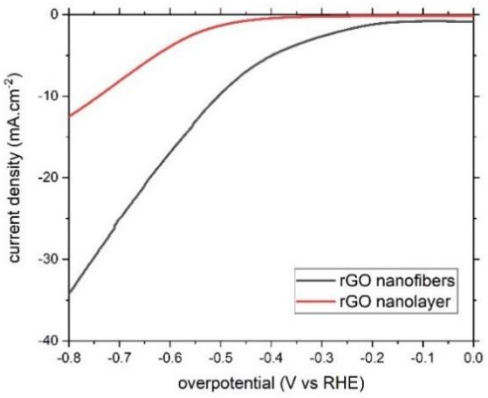

Figure 3.24. LSV curves of rGO nanofibers and rGO nanolayers.

While the rGO nanolayer on the FTO surface was peeled off after being stable up to a certain overpotential value during the LSV experiment, the rGO nanofibers remained stable on the FTO surface throughout the experiment and the experiments could be repeated. In addition, @10 mA cm^{-2}, it is seen that rGO NFs and nanolayers are at -505 and -730 mV overpotentials, respectively. GO NFs subjected to thermal reduction increased their adsorption capacity with temperature, enabling them to exhibit improved catalytic performance [113]. The fact that rGO was obtained in nanofiber form increased its extrinsic activity. In addition, Nafion was added to GO to improve layer stability before the GO suspension on the FTO surface was subjected to electrochemical reduction. Nafion dropped on GO decreased the electrical conductivity. Moreover, peeling off the GO layer from the FTO surface could not be prevented. While it was observed that the nanolayers were peeled off after being stable up to a certain overpotential value during the LSV experiment on the FTO surface, rGO nanofibers could remain stable on the FTO surface. In this respect, thermally reduced GO nanofibers have provided a great advantage in electrochemical experiments.

rGO and Ni/NiO NFs were electrospinned on the FTO surface ($rGO_{0.1}$ + Ni/NiO) under the same ambient conditions and using the same procedures. The LSV curves of the $rGO_{0.1}$ + Ni/NiO and $rGO_{0.1}$/Ni/NiO electrocatalysts are shown in Figure 3.25a. The $rGO_{0.1}$/Ni/NiO catalyst exhibited a steady increase in current density with increasing overpotential. Also, $rGO_{0.1}$/Ni/NiO exhibited higher reaction kinetics with a higher Tafel

slope of 147 mV dec^{-1} compared to NFs (Figure 3.25b). This can be attributed to the larger surface area of $rGO_{0.1}$/Ni/NiO heterostructured fibers and the synergistic effect between rGO and Ni/NiO. The close contact between Ni/NiO and rGO support provides enhanced structural stability of the electrocatalyst and thus improved HER performance.

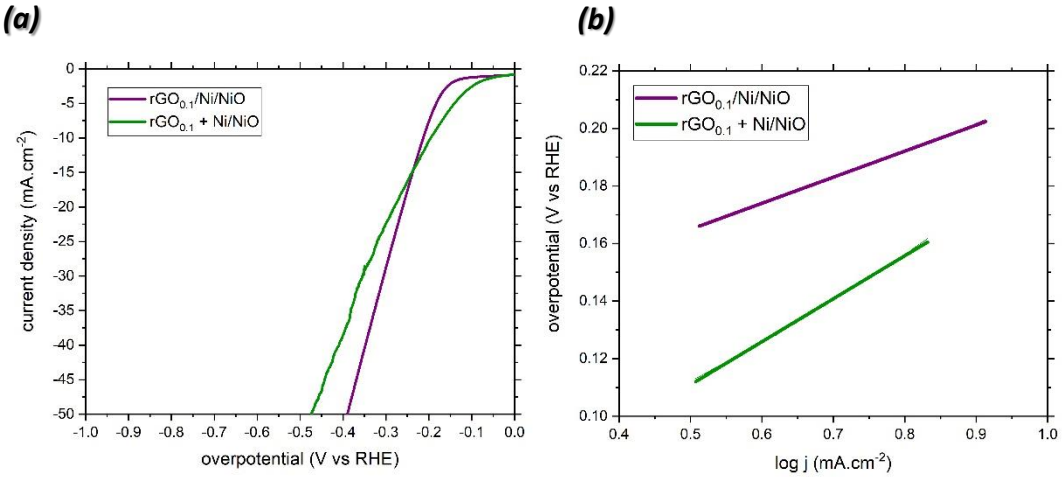

Figure 3.25 (a) LSV polarization curves of $rGO_{0.1}$ + Ni/NiO and $rGO_{0.1}$/Ni/NiO catalysts obtained at 10 mV s^{-1} in 1 M KOH (b) Tafel plots.

3.3.5 $rGO_{0.1}$/Ni/NiO electrocatalytic durability in alkaline electrolyte

The stability of the current density over time is an important parameter for long-term applications of catalysts. The long-term stability of Ni/NiO and $rGO_{0.1}$/Ni/NiO catalysts was tested by chronoamperometry (CA) experiment. Looking at the current-time graph of the Ni/NiO catalyst shown in Figure 3.26b, it was seen that the current density did not remain constant after 5 hours. This is because the Ni/NiO nanofibers peel off on the electrode surface and the electrode loses its stability. Besides, examining the CA experiment of the $rGO_{0.1}$/Ni/NiO electrocatalyst revealed that the current response was almost constant throughout the 10-hour stability test (Fig. 3.26a). The hydrogen generation capacity of the electrode did not change during this time.

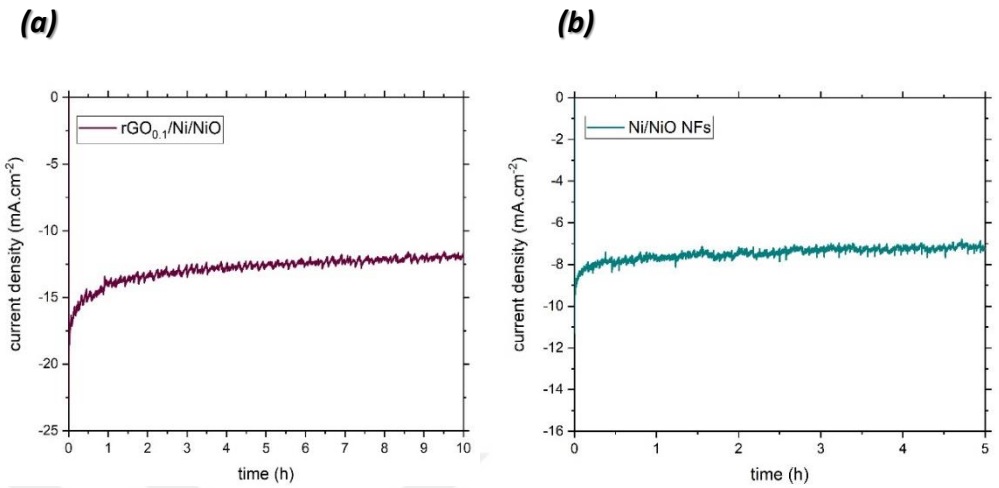

Figure 3.26 Chronoamperometry experiments of (a) $rGO_{0.1}$/Ni/NiO, and (b) Ni/NiO under constant potential of −0.3 V vs RHE in 1 M KOH.

After 10 hours, the LSV polarization curve of the $rGO_{0.1}$/Ni/NiO catalyst was recorded again. The polarization graphs before and after the stability test of the $rGO_{0.1}$/Ni/NiO catalyst are shown in Figure 3.27. It is seen that the polarization curves follow each other. Based on these results, we can say that the stability of the catalyst is quite good and the sample is another proof of long-term stability. It is clear from these durability tests that rGO improves the long-term stability of the electrode.

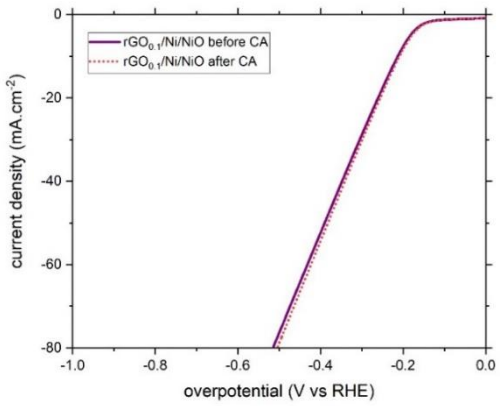

Figure 3.27 Linear sweep voltammograms of $rGO_{0.1}$/Ni/NiO $rGO_{0.1}$/Ni/NiO NFs before and after chronoamperometry.

Using the current density recorded throughout the chronoamperometry experiment, it is possible to calculate the theoretical amount of hydrogen produced. The calculated theoretical hydrogen production amount of Ni/NiO and $rGO_{0.1}$/Ni/NiO catalysts is given in Table 3.5. According to the current density recorded as a result of the same amount of potential given to the system, the theoretical amount of hydrogen produced was calculated as 0.06 and 0.015 mmol/h for Ni/NiO and $rGO_{0.1}$/Ni/NiO, respectively. The amount of hydrogen produced with the system using the $rGO_{0.1}$/Ni/NiO catalyst is more than twice the amount produced with Ni/NiO.

Table 3.5 Amount of theoretically produced hydrogen in 1 M KOH electrolyte.

	Potential (mV)	**H_2 produced (theoretical) (mmol/hr)**
Ni/NiO	-250	0.06
$rGO_{0.1}$/Ni/NiO	-250	0.15

After applying a constant potential of -0.3 V to the system for 10 hours, SEM images of the electrode were examined to observe the stability of the heterostructured NFs. As seen in Figure 3.28, there was no significant change in the morphology of the nanofibers after the chronoamperometry experiment. These results are promising for the long-term stability of the electrode.

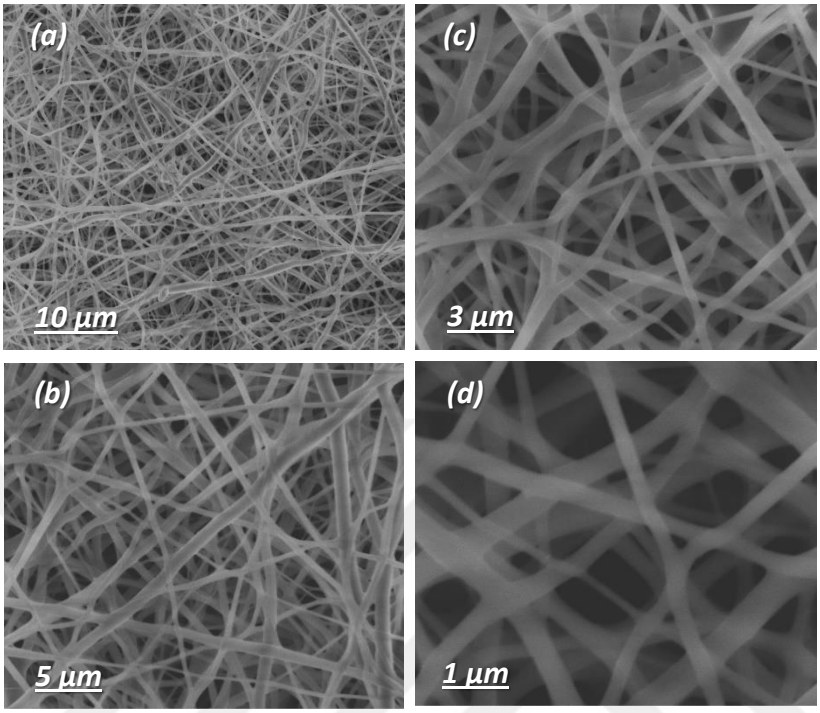

Figure 3.28 Low and high magniification SEM images of $rGO_{0.1}$/Ni/NiO catalysts after long-term stability test.

Chapter 4

Conclusion

In conclusion, $rGO_{0.1}$/Ni/NiO, Ni/NiO and rGO nanofibers were fabricated as electrocatalyst and their performances towards HER were investigated in alkaline electrolyte. These fibers were fabricated in two steps: (i) electrospinning and (ii) calcination. Parameters such as concentration/viscosity of the precursor, the applied voltage, the flow rate, the distance between collector and needle tip, the spinning duration and the calcination temperature of the fibers to be coated on the FTO surface were optimized. The HER performances of the electrodes were investigated by electrochemical experiments in alkaline electrolytes with different concentrations, it was observed that they showed the best electrocatalytic activity at 1 M KOH. Thus, electrochemical measurements such as linear sweep voltammetry (LSV), electrochemical impedance spectroscopy (EIS), chronoamperometry (CA), and cyclic voltammetry (CV) were performed in 1 M KOH electrolyte.

Different ratios of GO dispersions were added to PVA/Ni salt precursors and rGO_x/Ni/NiO heterostructures were obtained by calcining as-spun nanofibers obtained by electrospinning and thermal reduction of GO during calcination. After investigating whether the catalysts containing GO in different ratios were produced as equal nanofibers by SEM, their electrochemical performances were tested and $rGO_{0.1}$/Ni/NiO was determined as the optimum catalyst. The electrocatalytic activities of rGO, Ni/NiO and $rGO_{0.1}$/Ni/NiO were compared using polarization curves. Electrocatalysts reached the current density of 10 mA cm^{-2} at overpotentials of -505 mV, -260 mV and -212 mV, respectively. As a result, $rGO_{0.1}$/Ni/NiO nanofibers revealed the best catalytic activity

for HER. Tafel curves were used to investigate the kinetics of the catalysts. Comparing the Tafel slopes for rGO, Ni/NiO and $rGO_{0.1}$/Ni/NiO catalysts, it was seen that $rGO_{0.1}$/Ni/NiO had the lowest Tafel slope of 90.6 mV dec^{-1}. Based on these results, it was concluded that $rGO_{0.1}$/Ni/NiO has the most improved kinetics for HER. The results were consisstent with Nyquist plots where the R_{ct} value of Ni/NiO (123 Ω) was higher than that of $rGO_{0.1}$/Ni/NiO (52 Ω). As the presence of large surface area of rGO accelerated electron mobility, the charge transfer resistance was reduced to 52 Ω and $rGO_{0.1}$/Ni/NiO showed faster kinetics for HER. As a result of comparing our optimum sample with rGO and Ni/NiO fibers, it was observed that its electrocatalytic activity and stability were significantly improved compared to rGO and Ni/NiO.

In order to examine the effect of fabrication of the catalyst in heterostructured form on HER performance, rGO and Ni/NiO nanofibers were coated and calcined on the FTO surface, respectively. Comparing the rGO + Ni/NiO composite structure with $rGO_{0.1}$/Ni/NiO catalyst, it was observed that $rGO_{0.1}$/Ni/NiO has lower overpotential and higher HER kinetics. To observe the effect of fabrication of catalysts in nanofiber form, HER activities of rGO nanofibers and nanolayers were compared with linear sweep voltammetry, and it was seen that nanofibers had more positive overpotential value. These results revealed that the production of the catalyst in heterostructured nanofiber form significantly improved its extrinsic and intrinsic activity.

The durability of $rGO_{0.1}$/Ni/NiO and Ni/NiO fibers was tested by chronoamperometry experiment by applying a constant potential of 0.3 V vs RHE to the system at 1 M KOH. Ni/NiO fibers peeled off from the FTO surface after 5 hours, while $rGO_{0.1}$/Ni/NiO exhibited a nearly constant current density versus time after a 10-hour experiment with the presence of rGO in the heterostructure, demonstrating superior stability. Repeated linear sweep voltammetry after the chronoamperometry experiment also confirmed that the catalyst remained almost completely stable. The durability of the optimum catalyst has also been proven by SEM images after chronoamperometry.

Bibliography

[1] I. Dincer and A. S. Joshi, Solar Based Hydrogen Production Systems, 1st ed. Springer-Verlag New York, 2013.

[2] Reed S, Ewing J. (2021 July 15). Hydrogen is One Answer to Climate Change. Getting it is the Hard Part. New York Times. Retrieved from https://www.nytimes.com/2021/07/13/business/hydrogen-climate-change.html.

[3] X. Zou and Y. Yang, "Noble metal-free hydrogen evolution catalysts for water splitting," *Chem. Soc. Rev.*, 2015, vol. 44, pp. 5148-5180.

[4] J. E. Funk, "Thermochemical hydrogen production: past and present," *Int. J. Hydrog. Energy*, 2001, vol. 26, no. 3, pp. 185-190.

[5] H. Kaneko, N. Gokon, N. Hasegawa and Y. Tamaura, "Solar thermochemical process for hydrogen production using ferrites," *Energy*, 2005, vol. 30, no. 11-12, pp. 2171-2178.

[6] A.V. Levchenko, Y.A. Dobrovolsky and N.G. Bukun, "Chemical and electrochemical processes in low-temperature superionic hydrogen sulfide sensors," *Russ J Electrochem*, 2007, vol. 43, pp. 552–560.

[7] Y. Amao, Y. Tomonou and I. Okura, "Highly efficient photochemical hydrogen production system using zinc porphyrin and hydrogenase in CTAB micellar system," *Sol. Energy Mater. Sol. Cells*, 2003, vol. 79, no. 1, pp. 103-111.

[8] A.A. Nada, M.H. Barakat, H.A. Hamed, N.R. Mohamed and T.N. Veziroglu, "Studies on the photocatalytic hydrogen production using suspended modified TiO2 photocatalysts," *Int. J. Hydrog. Energy*, 2005, vol. 30, no 7, pp. 687-691.

[9] V. Sediroglu, I. Eroglu, M. Yücel, L. Türker and U. Gündüz, "The biocatalytic effect of Halobacterium halobium on photoelectrochemical hydrogen production," *J. Biotechnol*, 1999, vol. 35, pp. 115-124.

[10] H. Jin, Y. Xu, R. Lin and W. Han, "A proposal for a novel multi-functional energy system for the production of hydrogen and power," *Int. J. Hydrog. Energy*, 2008, vol. 33, no. 1, pp. 9-19.

[11] D. Wang, S. Czernik, D. Montané, M. Mann and E. Chornet, "Biomass to Hydrogen via Fast Pyrolysis and Catalytic Steam Reforming of the Pyrolysis Oil or Its Fractions," 1997, *Ind. Eng. Chem. Res*, vol. 36, no. 5, pp. 1507–1518.

[12] A. Demirbaş, "Yields of hydrogen-rich gaseous products via pyrolysis from selected biomass samples," *Fuel*, 2001, vol. 80, no. 13, pp. 1885-1891.

[13] M. F. Demirbaş, "Hydrogen from Various Biomass Species via Pyrolysis and Steam Gasification Processes," *Energy Sources,* 2006, vol. 28, no. 3, pp. 245-252.

[14] M. Saxe and P. Alvfors, "Advantages of integration with industry for electrolytic hydrogen production," *Energy,* 2007, vol. 32, no. 1, pp. 42-50.

[15] T. Kato, M. Kubota, N. Kobayashi and Y. Suzuoki, "Effective utilization of by-product oxygen from electrolysis hydrogen production," *Energy,* 2005, vol. 30, no. 14, pp. 2580-2595.

[16] W.G. Colella, M. Z. Jacobson and D. M. Golden, "Switching to a U.S. hydrogen fuel cell vehicle fleet: The resultant change in emissions, energy use, and greenhouse gases," *J. Power Sources*, 2005, vol. 150, pp. 150-181.

[17] P. Sun, B. Young, A. Elgowainy, Z. Lu, M. Wang, B. Morelli and T. Hawkins, "Criteria Air Pollutants and Greenhouse Gas Emissions from Hydrogen Production in U.S. Steam Methane Reforming Facilities," *Environ. Sci. Technol*, 2019, vol, 53, no. 12, pp. 7103–7113.

[18] Shaw, A. (2021 May 21). Hydrogen and the path to Net Zero, Sembcorp Energy, UK. Retrieved from https://www.sembcorpenergy.co.uk/blog/hydrogen-and-the-path-to-net-zero/

[19] Farmer M. (2021 April 1). What colour is your hydrogen? A power technology jargon-buster. London, UK: Power Technology; 2020. Retrieved from https://www.power-technology.com/features/hydrogen-power-blue-green-grey-brown-extraction-production-colour-renewable-energy-storage/.

[20] van Hulst N. (2019 April 23). The clean hydrogen future has already begun. IEA commentary, International Energy Agency. Retrieved from https://www.iea.org/commentaries/the-clean-hydrogen-future-has-already-begun.

[21] I. Dincer, "Green methods for hydrogen production," *Int. J. Hydrog. Energy*, 2012, vol. 37, no. 2, pp. 1954-1971.

[22] EIA. (2016 April 16), US Natural Gas Production Reaches Record High in 2015, Today in Energy, Energy Information Agency, U.S. Department of Energy. Retrieved from https://www.eia.gov/today inene rgy/detail.php?id=25832.

[23] EIA. (2021 October 29), US Natural Gas Total Consumption. Energy Information Agency, U.S. Department of Energy. Retrieved from https://www.eia.gov/dnav/ng/hist/n9140 us2A.htm.

[24] B. You and Y. Sun, "Innovative Strategies for Electrocatalytic Water Splitting," Acc. Chem. Res., vol. 51, no. 7, pp. 1571–1580, 2018.

[25] X. Zhou and Y. Zhang, "Noble metal-free hydrogen evolution catalysts for water splitting," *Chem. Soc. Rev*, 2015, vol. 44, pp. 5148-5180.

[26] Z. Feng, J. Pu, X. Zhang, W. Zhang, M. Liu, L. Cui and J. Liu, "Heterostructured CoO/Co3O4 nanowire array on Titanium mesh as efficient electrocatalysts for hydrogen evolution reaction," *J. Alloys Compd.* 2021, vol. 881, 160603.

[27] N. Furuya and S. Motoo, "The electrochemical behavior of ad-atoms and their effect on hydrogen evolution: Part III. Platinum ad-atoms on gold, and gold ad-atoms on platinum," *J. Electroanal. Chem. Interf. Electrochem.* 1978, Volume 88, no. 2, pp. 151-160.

[28] A. Kiani and S. Hatami, "Fabrication of platinum coated nanoporous gold film electrode: A nanostructured ultra-low-platinum loading electrocatalyst for hydrogen evolution reaction," *Int. J. Hydrog. Energy*, 2010, vol. 35, no. 11, pp. 5202-5209.

[29] H. Sun, Z. Ma, Y. Qiu, H. Liu and G. G. Gao, "Ni@NiO Nanowires on Nickel Foam Prepared via "Acid Hungry" Strategy: High Supercapacitor Performance and Robust Electrocatalysts for Water Splitting Reaction," *Small*, 2018, vol. 14, no. 31, 1800294.

[30] A.Y. Faid, A.O. Barnett, F. Seland and S. Sunde, Ni/NiO nanosheets for alkaline hydrogen evolution reaction: in situ electrochemical-Raman study, *Electrochim. Acta*, 2020, vol. 361, 137040.

[31] J. Wang, Z. Zhao, C. Shen, H. Liu, X. Pang, M. Gao, J. Mu, F. Cao and G. Li, "Ni/NiO heterostructures encapsulated in oxygen-doped graphene as multifunctional electrocatalysts for the HER, UOR and HMF oxidation reaction," *Catal. Sci. Technol.*, 2021, vol. 11, pp. 2480–2490.

[32] Strmcnik, D., Uchimura, M., Wang, C. et al. "Improving the hydrogen oxidation reaction rate by promotion of hydroxyl adsorption," *Nature Chem*, vol. 5, pp. 300–306, (2013).

[33] M. Gong, W. Zhou, M.-C. Tsai, J. Zhou, M. Guan, M.-C. Lin, B. Zhang, Y. Hu, D.-Y. Wang, J. Yang, S. J. Pennycook, B.-J. Hwang and H. C. Dai, "Metal oxide-based materials as an emerging family of hydrogen evolution electrocatalysts," *Nat. Commun.*, 2014, vol. 5, pp. 4695.

[34] A.G. Oshchepkov, A. Bonnefont, V.A. Saveleva, V. Papaefthimiou, S. Zafeiratos, S.N. Pronkin, V.N. Parmon and E.R. Savinova, "Hydrogen Oxidation on Ni-Based Electrocatalysts: The Effect of Metal Doping," *Top. Catal*. Vol. 59, pp. 1319–1331, (2016).

[35] S. Lu, M. Hummel, Z. Gu, Y. Gu, Z. Cen, L. Wei, Y. Zhou, C. Zhang, and C. Yang, "Trash to treasure: A novel chemical route to synthesis of NiO/C for hydrogen production," *Int. J. Hydrog. Energy*, 2019, vol. 44, no. 31, pp. 16144-16153.

[36] Subbaraman, R., Tripkovic, D., Chang, K.C. et al., "Trends in activity for the water electrolyser reactions on 3d M(Ni,Co,Fe,Mn) hydr(oxy)oxide catalysts," *Nature Mater*, vol. 11, pp. 550–557, (2012).

[37] M. Gong, W. Zhou, M. C. Tsai, J. Zhou, M. Guan, M. C. Lin, B. Zhang, Y. Hu, D. Y. Wang, J. Yang, S. J. Pennycook, B. J. Hwang and H. Dai, "Nanoscale nickel oxide/nickel heterostructures for active hydrogen evolution electrocatalysis," *Nat. Commun.* 2014, vol. 5, pp. 4695−4701.

[38] Choi S., Kim C., Suh J.M. and Jang H.W., "Reduced graphene oxide-based materials for electrochemical energy conversion reactions," *Carbon Energy*, 2019, vol. 1, pp. 85– 108.

[39] J. Bao, J. Wang, Y. Zhou, Y. Hu, Z. Zhang, T. Li, Y. Xue, C. Guo and Y. Zhang, Anchoring Ultrafine Pt-Ni Nanoparticles on N Doped Graphene for Highly Efficient Hydrogen Evolution Reaction. *Catal. Sci. Technol.* 2019, vol. 9, no. 18, pp. 4961−4969.

[40] Chen, C., Long, M., Xia, M. et al. “Reduction of graphene oxide by an in-situ photoelectrochemical method in a dye-sensitized solar cell assembly,” *Nanoscale Res. Lett.,* 2012, vol. 7, pp. 101.

[41] Novoselov, K., Geim, A., Morozov, S. et al. “Two-dimensional gas of massless Dirac fermions in graphene,” *Nature*, 2005, vol. 438, pp. 197–200.

[42] C. Lee, X. Wei, J. W. Kysar and J. Hone, “Measurement of the Elastic Properties and Intrinsic Strength of Monolayer Graphene,” *Science*, 2008, vol. 321, pp. 385–388.

[43] Loh, K., Bao, Q., Eda, G. et al. “Graphene oxide as a chemically tunable platform for optical applications,” *Nature Chem* vol., 2010, vol. 2, pp. 1015–1024.

[44] D. R. Dreyer, S. Park, C. W. Bielawski, and R. S. Ruoff, "The chemistry of graphene oxide," *Chem. Soc. Rev.*, 2010, vol. 39, pp. 228-240.

[45] Hummers W.S. Jr. and Offeman R.E. “Preparation of graphitic oxide,” *J Am Chem Soc.* 1958, vol. 80, no. 6, pp. 1339-1339.

[46] Kovtyukhova N.I., Ollivier P.J., Martin B.R. et al. “Layer-by-layer assembly of ultrathin composite films from micron-sized graphite oxide sheets and polycations,” *Chem Mater*, 1999 vol. 11 no. 3, pp. 771-778.

[47] Dreyer D.R., Park S., Bielawski C.W. and Ruoff R.S. “The chemistry of graphene oxide,” *Chem Soc Rev.* 2010, vol. 39, no. 1, pp. 228-240.

[48] Jeon J.M, Kim T.L, Shim Y.S, et al. “Microscopic evidence for strong interaction between Pd and graphene oxide that results in metal-decoration-induced reduction of graphene oxide,” *Adv Mater*, 2017, vol. 29, no. 15, pp. 1605929.

[49] Compton O. C. and Nguyen S. T. “Graphene oxide, highly reduced graphene oxide, and graphene: versatile building blocks for carbon-based materials,” *Small*, 2010, vol. 6, no. 6, pp. 711-723.

[50] Liu M, Yang L, Liu T, et al. “Fe_2P/reduced graphene oxide/Fe_2P sandwich-structured nanowall arrays: a high-performance non-noble-metal electrocatalyst for hydrogen evolution,” *J Mater Chem A.* 2017, vol. 5, no. 18, pp. 8608-8615.

[51] Ma J, Wang M, Lei G, et al. “Polyaniline derived N-doped carbon-coated cobalt phosphide nanoparticles deposited on N-doped graphene as an efficient electrocatalyst for hydrogen evolution reaction,” *Small*. 2018, vol. 14, no. 2, pp. 1702895.

[52] Z. Lei, L. Lu and X. S. Zhao, “The electrocapacitive properties of graphene oxide reduced by urea,” *Energy Environ. Sci.,* 2012, vol. 5, pp. 6391–6399.

[53] P. Song, X. Zhang, M. Sun, X. Cui and Y. Lin, “Electrochemically reduced graphene oxide with porous structure as a binder-free electrode for high-rate supercapacitors,” *RSC Adv.,* 2012, vol. 2, pp. 1168–1173.

[54] W. Chen, L. Yan and P. R. Bangal, “Preparation of graphene by the rapid and mild thermal reduction of graphene oxide induced by microwaves,” *Carbon,* 2010, vol. 48, pp. 1146– 1152.

[55] D. Long, W. Li, L. Ling, J. Miyawaki, I. Mochida and S.H. Yoon, “Preparation of nitrogen-doped graphene sheets by a combined chemical and hydrothermal reduction of graphene oxide,” *Langmuir,* 2010, vol. 26, pp. 16096–16102.

[56] H.B. Zhang, J.W. Wang, Q. Yan, W.G. Zheng, C. Chen and Z.Z. Yu, “Characterization of graphite oxide after heat treatment,” *J. Mater. Chem.,* 2011, vol. 21, pp. 5392–5397.

[57] X. Chen, G. Liu, W. Zheng, W. Feng, W. Cao, W. Hu, and P. Hu, “Vertical 2D MoO_2/$MoSe_2$ Core–Shell Nanosheet Arrays as High-Performance Electrocatalysts for Hydrogen Evolution Reaction,” *Adv. Funct. Mater.,* 2016, vol. 26, no. 46, pp. 8537-8544.

[58] Jaksic, M.M., “Hypo–hyper-d-electronic interactive nature of interionic synergism in catalysis and electrocatalysis for hydrogen reactions,” *Int J Hydrog Energy,* 2001, vol. 26 no. 6, pp. 559-578.

[59] Miles, M. and M. Thomason, “Periodic variations of overvoltages for water electrolysis in acid solutions from cyclic voltammetric studies,” *J. Electrochem. Soc.* 1976, vol. 123 no. 10, pp. 1459-1461.

[60] J. Huang, Y. Jiang, T. An and M. Cao, “Increasing the active sites and intrinsic activity of transition metal chalcogenide electrocatalysts for enhanced water splitting,” *J. Mater. Chem. A,* 2020, vol. 8, pp. 25465.

[61] J. D. Benck, T. R. Hellstern, J. Kibsgaard, P. Chakthranont, and T. F. Jaramillo, “Catalyzing the Hydrogen Evolution Reaction (HER) with Molybdenum Sulfide Nanomaterials,” *ACS Catal.* 2014, vol. 4, no. 11, pp. 3957–3971.

[62] R. D. Nikam, A. Y. Lu, P. A. Sonawane, U. R. Kumar, K. Yadav, L. J. Li and Y. T. Chen, "Enhanced charge transport in ReSe2-based 2D/3D electrodes for efficient hydrogen evolution reaction," *ACS Appl Mater Interfaces*, 2015, vol. 7, pp. 23328.

[63] Q. Qu, J. H. Zhang, J. Wang, Q. Y. Li, C. W. Xu and X. Lu, "Three-dimensional ordered mesoporous Co3O4 enhanced by Pd for oxygen evolution reaction," *Sci. Rep.* 2017, vol. 7, pp. 41542.

[64] Chen H., Ge D., Chen J., Li R., Zhang X., Yu T., Wang Y. and Song S., "In Situ Surface Reconstruction Synthesis of a Nickel Oxide/ Nickel Heterostructural Film for Efficient Hydrogen Evolution Reaction," *Chem. Commun.* 2020, vol. 56, pp. 10529−10532.

[65] M. S. Faber, R. Dziedzic, M. A. Lukowski, N. S. Kaiser, Q. Ding, and S. Jin, "High-Performance Electrocatalysis Using Metallic Cobalt Pyrite (CoS_2) Micro- and Nanostructures," *J. Am. Chem. Soc.* 2014, vol. 136, no. 28, pp. 10053–10061.

[66] Z.-M. Huang, Y.-Z. Zhang, M. Kotaki and S. Ramakrishna, "A review on polymer nanofibers by electrospinning and their applications in nanocomposites.," *Composites Science and Technology,* 2003, vol. 63, pp. 2223–2253.

[67] W. Teo and S. Ramakrishna, "A review on electrospinning design and nanofiber assemblies," *Nanotechnology*, 2006, vol. 17, pp. 89–106.

[68] A. Greiner and J. H. Wendorff, "Electrospinning: A Fascinating Method for the Preparation of Ultrathin Fibers," 2007, *Angew. Chem., Int. Ed.,* vol. 46, pp. 5670-5703.

[69] D. Li and Y. Xia, "Electrospinning of Nanofibers: Reinventing the Wheel?" *Adv. Mater., 2004,* vol. 16, no. 14, pp. 1151–1170.

[70] G. R. Mitchell, K. H. Ahn and F. J. Davis, "The potential of electrospinning in rapid manufacturing processes," *Virtual Phys. Prototyp.,* 2011, vol. 6, no. 2, pp. 63–77.

[71] W. E. Teo and S. Ramakrishna, "A review on electrospinning design and nanofibre assemblies," 2006, *Nanotechnology*, vol. 17, no. 14, pp. R89–R106.

[72] S. Ramakrishna, K. Fujihara, W.E. Teo, T. Yong, Z. Ma and R. Ramaseshan, "Electrospun nanofibers: solving global issues," *Materials Today,* 2006, vol. 9, no. 3, pp. 40-50.

[73] Nathanael A. J. and Oh T.H., "Encapsulation of Calcium Phosphates on Electrospun Nanofibers for Tissue Engineering Applications," *Crystals*, 2021, vol.11, pp. 199.

[74] J. H. Kim, B. J. Park and Y. W. Han, “Evaluation of fatigue characteristics for adhesively-bonded composite stepped lap joint,” *Compos. Struct.*, 2004, vol. 66, pp. 69-75.

[75] Furuya N., Yamazaki T. and Shibata M., “High performance Ru-Pd catalysts for CO_2 reduction at gas-diffusion electrodes,” *J. Electroanal. Chem*. 1997, vol. 431, pp. 39–41.

[76] Hara K. and Sakata T. “Electrocatalytic formation of CH_4 from CO_2 on a Pt gas diffusion electrode.” *J. Electrochem. Soc*. 1997, vol. 144, pp. 539–545.

[77] Wang Z.M., Liu P., Cao Y.P., Ye F., Xu C. and Du X.Z., “Characterization and electrocatalytic properties of electrospun Pt-IrO_2 nanofiber catalysts for oxygen evolution reaction.” *Internat. J. Energy Res.* 2021, vol. 45, pp. 5841–5851.

[78] A.Q. Mugheri, S. Ali, G.S. Narejo, A.A. Otho, R. Lal, M.A. Abro, S.H. Memon and F. Abbasi, “Electrospun fibrous active bimetallic electrocatalyst for hydrogen evolution*.” Internat. J. Hydrogen Energy* 2020, vol. 45, pp. 21502–21511.

[79] Sankar S.S., Karthick K., Sangeetha K., Gill R.S. and Kundu S., “Annexation of nickel vanadate ($Ni_3V_2O_8$) nanocubes on nanofibers: An excellent electrocatalyst for water oxidation.” *ACS Sustain. Chem. Eng.* 2020, vol. 11, pp. 4572–4579.

[80] G. Issabayeva, M.K. Aroua and N.M. Sulaiman, “Electrodeposition of copper and lead on palm shell activated carbon in a flow through electrolytic cell.” *Desalination*, 2006, vol. 194, pp. 192–201.

[81] Y. Abghou, S.B. Sigtryggsson and E. Skúlason, “Biomimetic nitrogen fixation catalyzed by transition metal sulfide surfaces in an electrolytic cell.” *ChemSusChem* 2019, vol. 12, pp. 4265–4273.

[82] J.Y. Jeong, H.K. Kim, J.H. Kim and J.Y. Park, “Electrochemical removal of nitrate using ZVI packed bed bipolar electrolytic cell,” *Chemosphere*, 2012, vol. 89, pp. 172–178.

[83] A. Chinnappan, J. Dongxiao, W. Jayathilaka, C. Baskar and X. Qin, “Facile synthesis of electrospun C@NiO/Ni nanofibers as an electrocatalyst for hydrogen evolution reaction,” *Int. J. Hydrogen Energy* 2018, vol. 43, pp. 15217-15224.

[84] A.Q. Mugheri, S. Ali, G.S. Narejo, A.A. Otho, R. Lal, M.A. Abro, S.H. Memon and F. Abbasi, “Electrospun fibrous active bimetallic electrocatalyst for hydrogen evolution,” *Internat. J. Hydrogen Energy*, 2020, vol. 45, pp. 21502–21511.

[85] J.G. Chen et al. “Best practices in pursuit of topics in heterogeneous electrocatalysis.” *ACS Catal*, 2017, vol. 7, no. 9, pp. 6392–6393.

[86] B.Y. Chang and S.M. Park, “Electrochemical Impedance Spectroscopy,” *Annu. Rev. Anal. Chem.*, 2010, vol. 3, pp. 207–229.

[87] Barai, A., Uddin, K., Widanage, W.D. et al. “A study of the influence of measurement timescale on internal resistance characterisation methodologies for lithium-ion cells.” *Sci. Rep.*, 2018, vol. 8, no. 21.

[88] Muralidharan, V.S., "Warburg impedance - basics revisited", *Anti-Corros Method M.*, 1997, Vol. 44 No. 1, pp. 26-29.

[89] L. Shahriary and A.A. Athawale, “Graphene oxide synthesized by using modified Hummers approach,” *Int. J. Renew Energy Environ Eng*, 2014, vol. 2, no. 1, pp. 58-63.

[90] Z. Mo, Y. Sun, H. Chen, P. Zhang, D. Zuo and Y. Liu, “Preparation and characterization of a PMMA/$Ce(OH)_3$, Pr_2O_3/graphite nanosheet composite,” *Polymer* 2005, vol. 46, no. 26, pp. 12670–12676.

[91] H. L. Guo, X. F. Wang, Q.Y. Qian, F.B. Wang and X.H. Xia, “A green approach to the synthesis of graphene nanosheets,” *ACS Nano*, 2009, vol. 3, no. 9, pp. 2653–2659.

[92] T.Y. Zhang and D. Zhang, “Aqueous colloids of graphene oxide nanosheets by exfoliation of graphite oxide without ultrasonication,” *Bull Mater Sci*, 2011, vol. 34, no. 1, pp. 25–28.

[93] Saxena S., Tyson T. A., Shukla S., Negusse E., Chen H. and Bai J., “Investigation of structural and electronic properties of graphene oxide,” *J. Appl. Phys. Lett.* 2011, vol. 99, no. 1, pp. 013104.

[94] Y. Wu, M. Huang, N. Song and W. Hu, “Electrochemical detection of guaiacol in bamboo juice based on the enhancement effect of RGO nanosheets,” 2014, *Anal. Methods*, vol. 6, pp. 2729–2735.

[95] C. Hontoria-Lucas, A. J. López-Peinado, J.de D. López-González, M. L. Rojas-Cervantes and R. M. Martín-Aranda, “Study of oxygen-containing groups in a series of

graphite oxides: Physical and chemical characterization," *Carbon*, 1995, vol. 33, no. 11, pp. 1585–1592.

[96] Cimenez V., Mantecon A. and Cadiz V., "Modification of Poly(vinyl alcohol) with Acid Chlorides and Crosslinking with Difunctional Hardeners." *J. Polym. Sci. Part A* 1996, vol. 34, pp. 925–934.

[97] Yu Y.H., Chan C.C., Lai, Y.C., Lin Y.Y., Huang Y.C., Chi W.F., Kuo C.W., Lin H.M. and Chen P.C., "Biocompatible Electrospinning Poly(vinyl alcohol) Nanofibres Embedded with Graphene-Based Derivatives with Enhanced Conductivity, Mechanical Strength and Thermal Stability." *RSC Adv.* 2014, vol. 4, pp. 56373−56384.

[98] Wu Y., Huang M., Song N. and Hu W., "Electrochemical detection of guaiacol in bamboo juice based on the enhancement effect of RGO nanosheets." *Anal Methods*, 2014, vol. 6, pp. 2729–2735.

[99] R. M. Ding, J. P. Liu, J. Jiang, F. Wu, J. H. Zhu and X. T. Huang, "Tailored Ni–Cu alloy hierarchical porous nanowire as a potential efficient catalyst for DMFCs," *Catal. Sci. Technol.*, 2011, vol. 1, pp. 1406–1411.

[100] H. Yan, Y. Xu, S. Jiang, J. Zou and W. Liang, "A fault tolerant control strategy for six-phase transverse flux tubular PMLM based on synthetic vector method," 2014, *17th International Symposium on Electromagnetic Launch Technology*, 2014, pp. 1-7.

[101] M. Iliut, C. Leordean, V. Canpean, C.M. Teodorescu, and S. Astilean, "A new green, ascorbic acid-assisted method for versatile synthesis of Au-graphene hybrids as efficient surface-enhanced Raman scattering platforms," *J. Mater. Chem. C*, 2013, vol. 1, no. 26, pp. 4094 - 4104.

[102] D. He, L. Shen, X. Zhang, Y. Wang, N. Bao, and H. H. Kung, "An efficient and eco-friendly solution-chemical route for preparation of ultrastable reduced graphene oxide suspensions," *J. AIChE. J.* 2014, vol. 60, no. 8, pp. 2757-2764.

[103] L. G. Cançado, A. Jorio, E. H. M. Ferreira, C. A. Achete, R. B. Capaz, and A. C. Ferrari, "Quantifying Defects in Graphene via Raman Spectroscopy at Different Excitation Energies," *J. Nano Lett.*, 2011, vol. 11, no. 8, pp. 3190-3196.

[104] Cho J. S., Lee S. Y., Ju H. S. and Kang Y. C., "Synthesis of NiO nanofibers composed of hollow nanospheres with controlled sizes by the nanoscale kirkendall

diffusion process and their electrochemical properties," *Acs. Appl. Mater. Inter.* 2015, vol. 7, no. 46, pp. 25641–25647.

[105] Baige Yuan et al, "Investigation into electrochemical performance of NiO/graphene composite nanofibers synthesized by a simple method as anode materials for high-performance lithium ion batteries," 2020, *Mater. Res. Express*, vol. 7, no. 11, 115007.

[106] P. Kiselev and J. R. Liompart, "Highly aligned electrospun nanofibers by elimination of the whipping motion," *J. Appl. Polymer Sci.*, 2012, vol. 125, no. 3, pp. 2433-2441.

[107] Dinh, C. T. et al. "Multi-site electrocatalysts for hydrogen evolution in neutral media by destabilization of water molecules." *Nat. Energy*, 2019, vol. 4, pp. 107–114.

[108] Zhou, K.L., Wang, Z., Han, C.B. et al. "Platinum single-atom catalyst coupled with transition metal/metal oxide heterostructure for accelerating alkaline hydrogen evolution reaction." *Nat Commun*, 2021, vol. 12, 3783.

[109] A.E.G.B. Gorospe, and M.D.L. Balela, "Ni-Co nanocomposites deposited on carbonfiber paper as an electrocatalyst towards hydrogen evolution reaction," *Mater. Today Proc.* 2020, vol. 22, pp. 255-261.

[110] S. Badrayyana, D.K. Bhat, S. Shenoy, Y. Ullal and A.C. Hegde, "Novel Fe–Ni-Graphene composite electrode for hydrogen production," *Int. J. Hydrogen Energy*, 2015, vol. 40, no. 33, pp. 10453-10462.

[111] Z. H. Chen, Z. P. Ma, J. J. Song, L. X. Wang and G. J. Shao, "Novel one-step synthesis of wool-ball-like Ni-carbon nanotubes composite cathodes with favorable electrocatalytic activity for hydrogen evolution reaction in alkaline solution*," J. Power Sources*, 2016, vol. 324, pp. 86-96.

[112] L.J. Yang, X.C. Zhao, R.Z. Yang, P.X. Zhao, Y.T. Li, P. Yang, J.C. Wang and D. Astruc, "In-situ growth of carbon nanotubes on Ni/NiO nanofibers as efficient hydrogen evolution reaction catalysts in alkaline media," 2019, *Appl. Surf. Sci*. vol. 491, pp. 294–300.

[113] Z. G. Bajestani, A. Yürüm and Y Yürüm, "Significant improvement in the hydrogen storage capacity of a reduced graphene oxide/TiO_2 nanocomposite by chemical bonding of Ti–O–C," *RSC Adv*., 2016, vol. 6, pp. 32831-32838.